THE JOURNAL OF PHYSICAL CHEMISTRY Letters

pubs.acs.org/JPCL Letter

Hydrogen-Enhanced Vacancy Diffusion in Metals

Jun-Ping Du, W. T. Geng, Kazuto Arakawa, Ju Li,* and Shigenobu Ogata*

Cite This: J. Phys. Chem. Lett. 2020, 11, 7015−7020 Read Online

ACCESS | Metrics & More | Article Recommendations | Supporting Information

ABSTRACT: Vacancy diffusion is fundamental to materials science. Hydrogen atoms bind strongly to vacancies and are often believed to retard vacancy diffusion. Here, we use a potential-of-mean-force method to study the diffusion of vacancies in Cu and Pd. We find H atoms, instead of dragging, enhance the diffusivity of vacancies due to a positive hydrogen Gibbs excess at the saddle-point: that is, the migration saddle attracts more H than the vacancy ground state, characterized by an activation excess $\Gamma_H^m \approx 1$ H, together with also-positive migration activation volume Ω^m and activation entropy S^m. Thus, according to the Gibbs adsorption isotherm generalized to the activation path, a higher μ_H significantly lowers the migration free-energy barrier. This is verified by *ab initio* grand canonical Monte Carlo simulations and direct molecular dynamics simulations. This trend is believed to be generic for migrating dislocations, grain boundaries, and so on that also have a higher capacity for attracting H atoms due to a positive activation volume at the migration saddles.

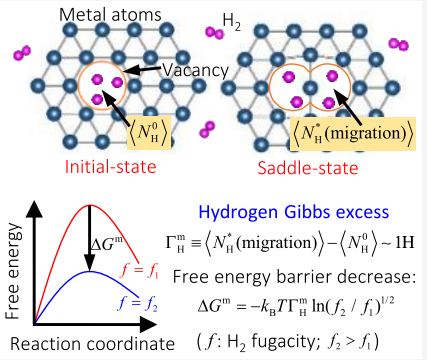

Hydrogen can either be an intentional constituent or unwelcome impurity in materials.[1] As a deliberate ingredient, a high concentration of H can cause the metal−H systems to function as energy-storage media,[2,3] sensors,[4] or catalysts.[5,6] Hydrogen is also notorious for degrading the mechanical properties of metals, in the form of hydrogen embrittlement[7−9] and hydrogen blistering/bubbling.[10−12] Hydrogen (tritium) is inevitably introduced into metals during forming, finishing operations, and radiation and environmental exposures, in for example nuclear fission and fusion power plant components. Due to the high mobility even at room temperature, H atoms can reach and achieve thermodynamic equilibrium quickly around the structural defects in metals,[1] such as vacancies, dislocations, and grain boundaries, changing their stability and mobility.

Transition-state theory[13] (TST), also referred to as activated-complex theory, is used to model the rate of system jumping from one free-energy minimum to another. The stress and temperature dependence of the jump rate (R) are characterized by the activation volume (ΔV^*) and the activation entropy (ΔS^*), respectively, that is

$$R = \nu_0 \exp\left(-\frac{\Delta U^* + P\Delta V^* - T\Delta S^*}{k_B T}\right) \quad (1)$$

where ν_0 is the attempt frequency, ΔU^* is the potential energy difference between the reactants (initial state) and the activated transition-state complex (saddle state, often denoted by the superscript *), P is the stress, T is the temperature, and k_B is Boltzmann's constant. The diffusive transport of metal atoms (M) in crystalline materials is dominated by the vacancy-exchange mechanism[14,15] and was studied based on TST using computational techniques for searching the minimum energy pathway (MEP). A key question is how to treat hydrogen segregation, i.e., do we consider the number of hydrogen (N_H) in the activated complex to be constant during the migration process, or do we allow it to vary? A careful examination of TST in the statistical sense indicates that it should be the latter. That is, we should allow N_H to be adjusted also (in the statistical kinetics sense), giving rise to a migration activation excess $\Gamma_H^m \equiv \langle \Delta N_H^*(\text{migration}) \rangle$ in the notation of the Gibbs adsorption isotherm

$$dG^m = -\Gamma_H^m d\mu_H + \Omega^m dP - S^m dT \quad (2)$$

for the migration free-energy barrier G^m, parallel to the definition of the migration activation volume $\Omega^m \equiv \Delta V^*(\text{migration}) \equiv V_{saddle}(T, P, \mu_H) - V_{initial}(T, P, \mu_H)$ and activation entropy $S^m \equiv \Delta S^*(\text{migration}) \equiv S_{saddle}(T, P, \mu_H) - S_{initial}(T, P, \mu_H)$.

Hydrogen atoms tend to segregate in the vacancy, often offset from the site center. This behavior of the H−vacancy complex has been explained by the effective medium theory,[16] which indicates that the energy needed to introduce H atoms into a background electron density, known as the embedding energy, achieves an optimal value at a preferred background electron density; thus, H atoms seek spots with such preferred electron density on the outer surface and inner interstices of the metal. The mobility of H−vacancy complexes has been

Received: June 10, 2020
Accepted: July 30, 2020
Published: July 30, 2020

https://dx.doi.org/10.1021/acs.jpclett.0c01798
J. Phys. Chem. Lett. 2020, 11, 7015−7020

studied using the TST and first-principles calculations, often adopting M−V^0 distance as the reaction coordinate, where V^0 denotes the original vacancy site. Previous first-principles calculations based on density functional theory (DFT) have indicated that the H atoms trapped by vacancies can substantially increase the energy barrier to metal−vacancy exchange,[17,18] if N_H is fixed. Particularly, the ratio of the vacancy diffusion coefficient with and without H in a Ni−H system, D^V_{NiH}/D^V_{Ni}, decreases dramatically with increasing H-concentration, and the ratio can be as low as 10^{-4} at $c_H = 0.1$ (H-concentration in atomic ratio) and 700 K based on the DFT calculations.[17] This is based on the argument that during the rare but violent multiphonon-collisional atomic dynamics of thermally activated processes at picosecond time scale, there is sufficient time for the N_H hydrogens surrounding the activated complex to adjust their positions but no time for other hydrogens far way to arrive and have an effect during this migration, which is certainly true. Such a fixed-N_H argument, however, neglects the fact that there is not just one path but many possible activation paths that could lead to vacancy exchange. Indeed, the optimal N^*_H(migration) that minimizes the absolute Helmholtz free energy of the vacancy-exchange saddle-point is unlikely to be the N_H that optimizes the absolute Helmholtz free energy of the ground state, when this vacancy is immersed in a large hydrogenated crystal bath. So one can imagine the configuration having N^*_H instead of N_H hydrogen prepositioned in the vacancy (which is certainly not optimal and thus an excited configurational state), which then undergoes multiphonon-collision actuated atomic dynamics. By going through this excited precursor state with a chemical excess different from the ground-state configuration, one can then end up with the lowest absolute energy activated complex and therefore the largest TST rate contribution, more than the $N_H = N^0_H$ path, where superscript 0 is used to denote the ground-state optimum. In above, N^0_H and N^*_H are integers. By summing up all path contributions with various N_H, one can derive a Gibbs free-energy barrier, with $\Gamma^m_H \equiv \Gamma^*_H - \Gamma^0_H \equiv \langle N^*_H(\text{migration})\rangle - \langle N^0_H\rangle$, where Γ^*_H and Γ^0_H are statistical averages in the sense of the Gibbs adsorption isotherm[19,20] (Figure 1), $dG = -\Gamma_H d\mu_H + \Omega dP - SdT$ for the ground- and saddle-state respectively, and each can be a noninteger. Unlike traditional surface/interfacial excess, here we choose not to normalize mass excess versus an area (or length), because the vacancy is not an extended defect.

We would like to show conceptually that Γ^m_H is usually positive, just like the migration activation volume Ω^m (symbolizing dilation or extra free volume[21] during migration) and activation entropy $S^m > 0$ (symbolizing vibrational mode softening, as indicated by the Meyer−Neldel compensation rule[22,23] with positive T_{MN}). We can define a scalar reaction coordinate ξ based on the M−V^0 distance (d): $\xi \equiv 1 - d/d_{max}$. $\xi = 0$, 1 denotes the initial and final states, both perfect vacancies, while $\xi = 0.5$ denotes the saddle-point state, which is known both experimentally and from first-principles calculations to have a larger free volume and is vibrationally softer on average even after the imaginary-frequency phonon mode along the MEP is taken out. As illustrated in Figure 1, as M moves half way between the V^0 and V^1 sites, there is crowding between M and metal atoms, forcing an outward expansion of those metal atoms, enlarging the total volume ($\Omega^m > 0$). But also, both V^0 and V^1 site centers are effectively vacated, leaving significantly larger "internal surface areas" for hydrogen atoms to experience the optimal background electron density. It is

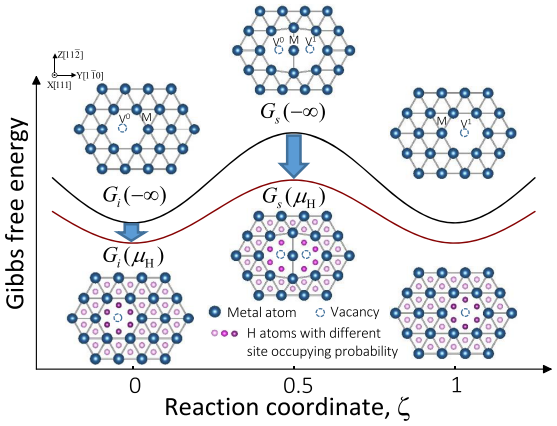

Figure 1. Schematics of Gibbs free-energy changes of the vacancy diffusion as a function of reaction coordinate in pure metals (black line) and a metal−H system (dark red line) under a specific H-concentration corresponding to a specific chemical potential of H (μ_H). The blue balls in the insets are metal atoms on one (111) plane with one vacancy. The small balls in the insets are H atoms in the interstitial sites colored by the site occupying probability. The metal atom, labeled by M, moves from the final vacancy site (V^1 at $\xi = 1$) to the initial vacancy site (V^0 at $\xi = 0$), while at the saddle-point state ($\xi = 0.5$), both V^0 and V^1 are effectively vacant and are able to trap more H atoms overall.

therefore natural to suspect $\Gamma^m_H > 0$ due to the larger H-trapping capacity of the activated complex. Thus, if the activation excess $\Gamma^m_H = 1$ H, for every 10× increase in equivalent hydrogen gas partial pressure (fugacity) P_{H_2}, we would predict a ($\sqrt{10} \approx 3.162\times$) increase in vacancy mobility, regardless of temperature. Note that generally speaking, Γ^m_H is temperature-dependent (see Secs. S2 and S8 in the Supporting Information). We term such hydrogen-dependent defect mobility the "hydrogen lubrication" effect, which could be operative for dislocations as well as grain boundaries.

Here, we performed the potential-of-mean-force[24] (PMF) calculations, *ab initio* grand canonical Monte Carlo (GCMC) simulations, and direct molecular dynamics (MD) simulations, to study the vacancy diffusivity under different H-concentrations, exploring the correlation between the diffusivity of the vacancy and the chemical composition variation of H along the vacancy diffusion pathway. Moreover, we choose Cu−H and Pd−H as prototype systems, since a large amount of H can be incorporated in the metals via high H_2 pressure[25] or an electrodeposition process.[26] For example, the H fraction in Pd (H to metal atomic ratio) can reach 0.7 under a H_2 pressure of 2 GPa,[27] and 0.02 through electrodeposition.[28]

To clarify the effect of chemical composition variation along the vacancy diffusion pathway, we computed the free-energy barrier by the integral of the time-averaged force on the jumping metal atom over the reaction coordinates of the vacancy diffusion from the initial energy minimum to the saddle state based on the PMF method with the embedded-atom-method (EAM) potentials[29−31] (see Secs. S3 and S9 in the Supporting Information). On the basis of the TST, the jump frequency (R) is given by $R = \upsilon_0 \exp(-G^m/k_BT)$, where υ_0 is the attempt frequency, and G^m is the free-energy barrier for the vacancy jump as computed using the PMF simulations. The uncorrelated diffusion coefficient of vacancy is estimated by[32] $D^V = a_0^2 R$, where a_0 is the lattice constant. Assuming the same υ_0 for the pure metal and metal−H systems, the vacancy

https://dx.doi.org/10.1021/acs.jpclett.0c01798
J. Phys. Chem. Lett. 2020, 11, 7015−7020

diffusion coefficient ratios with and without H at 870 K from the PMF simulation are computed using $D^{V}_{MH}/D^{V}_{M} = \exp(-\Delta G^{m}/k_{B}T)$ and shown in Figure 2(a,b), where M = Cu or Pd, and $\Delta G^{m} = G^{m} - G^{m}_{0}$ is the difference of free-energy barrier between the M−H system (G^{m}) and pure M system (G^{m}_{0}). From Figure 2(a,b), for $c_H > 0.01$, the PMF surprisingly predicts a diffusivity substantially greater than that in pure Cu and Pd (e.g., $D^{V}_{CuH}/D^{V}_{Cu} \approx 12$ at $c_H = 0.2$). Next, we computed the number of H atoms adsorbed in the initial ($\Gamma^{0}_{H} \equiv \langle N^{0}_{H}\rangle$) and the saddle ($\Gamma^{*}_{H} \equiv \langle N^{*}_{H}(\text{migration})\rangle$) states. In an FCC lattice with a single vacancy, eight first-nearest-neighbor tetragonal [1NN(T)] and six second-nearest-neighbor octahedral [2NN(O)] interstitial sites are located near the vacancy center of V^0 and V^1. According to the interaction energy between the H atom and the vacancy, the H atoms within 2NN(O) from the vacancy center of V^0 are counted as Γ^{0}_{H} in the initial state (see Sec. S4 and Figures S7 and S8 in the Supporting Information). Whereas, in the saddle-point state, the H atoms within 2NN(O) from the vacancy centers of both V^0 and V^1 can be counted as Γ^{*}_{H}. The results of Γ^{0}_{H} and Γ^{*}_{H} are shown in Figure 2(c,d), respectively. We can see that Γ^{*}_{H} is more than Γ^{0}_{H} but less than the twice of that ($2\Gamma^{0}_{H} > \Gamma^{*}_{H} > \Gamma^{0}_{H}$). This means that while the additional H atoms are adsorbed near V^1 at the saddle-point state, some H atoms are also squeezed out from V^0. But, the total number of the adsorbed H in the saddle state is more than that in the initial state.

Ab initio GCMC simulation is a reliable method to explore the surface structures and compositions.[33] To further validate the generally positive activation excess $\Gamma^{m}_{H} \equiv \Gamma^{*}_{H} - \Gamma^{0}_{H} \approx 1$ H in vacancy migration, we performed *ab initio* GCMC simulations in the Cu−H and the Pd−H systems to compute Γ^{0}_{H} and Γ^{*}_{H} in the ground and the saddle states of vacancy migration, respectively (see Sec. S5 in Supporting Information). To reduce the computational cost, the thermal movements of metal atoms and the thermal expansion of the lattice are ignored in most of the simulations, while the H atoms are only moved and inserted/deleted in the region of the "internal surface" of the vacancy (Figure 3(a)) under a specific μ_H and a constant temperature of 870 K. Figure 3(b,c) reveals that the Γ^{*}_{H} in the saddle-state is larger than the Γ^{0}_{H} in the ground-state for the Cu−H and Pd−H systems, that is, $\Gamma^{m}_{H} > 0$ (Figure 3(d)), which is consistent with the results of PMF method with EAM potentials. We have confirmed that ignoring the thermal expansion of lattice and the thermal movements of metal atoms does not change the above conclusion, by performing additional simulations considering these effects (see also Figure S1 and Sec. S5 in the Supporting Information).

In order to more directly demonstrate the dynamical process of diffusion of vacancies, we performed a series of MD simulations with EAM potentials at 870 K and at different H fractions ranging from 0 to 0.3 for Cu−H and Pd−H systems (see Sec. S6 in Supporting Information). The results of the vacancy diffusion coefficient ratios with and without H, D^{V}_{CuH}/D^{V}_{Cu} and D^{V}_{PdH}/D^{V}_{Pd}, are also shown in Figure 2(a,b), respectively. We can see that the H-enhanced vacancy diffusion from the direct MD simulations is in good agreement with those from the PMF method. A direct comparison of the vacancy diffusion under the higher and the lower H-concentrations is shown in the Supporting Information,

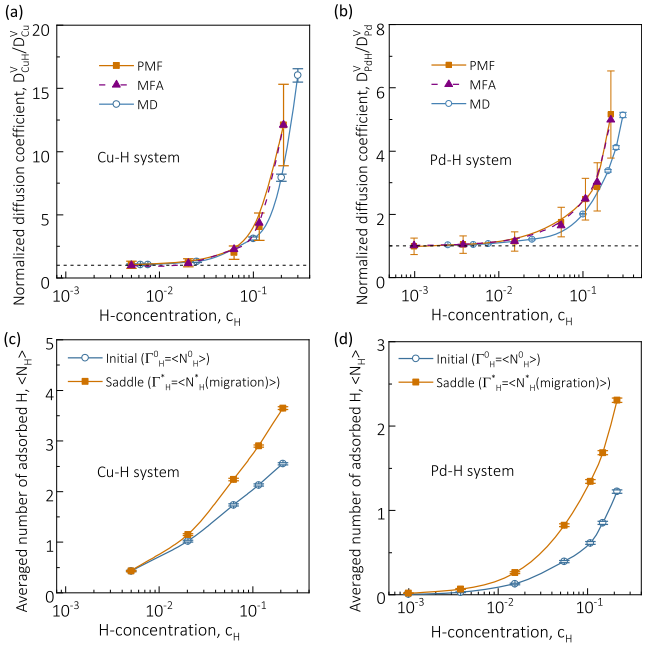

Figure 2. Vacancy diffusivity and the chemical composition variation of H along the vacancy diffusion pathway in a metal−H system. (a) and (b) manifest the ratio of the vacancy diffusion coefficient in the metal−H system to that in the pure metal system at 870 K computed from the potential-of-mean-force (PMF) method, an analytic expression under a mean field approximation (MFA) and direct MD method. (c) and (d) show the number of adsorbed H atoms at the initial and the saddle states as computed from the PMF method. The error bars in (a−d) are standard error of the data.

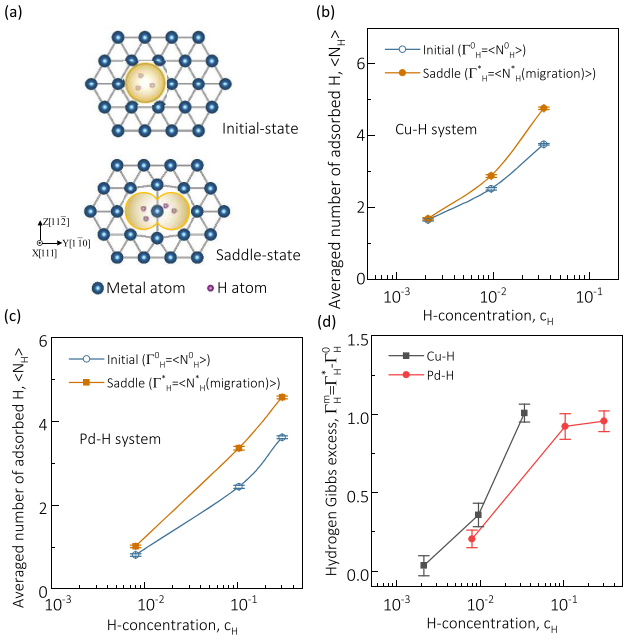

Figure 3. (a) Schematics of the initial and the saddle states used in *ab initio* GCMC simulations. The blue balls are metal atoms on one (111) plane with one vacancy. The small balls are H atoms, which are inserted in the "internal surface" regions of the vacancy (spherical, yellow regions). (b) and (c) show the averaged number of adsorbed H atoms at the initial and the saddle states at 870 K in Cu−H and Pd−H systems, respectively. (d) manifests the hydrogen Gibbs excess as computed. The error bars in (b−d) are the standard error of the data.

https://dx.doi.org/10.1021/acs.jpclett.0c01798
J. Phys. Chem. Lett. 2020, 11, 7015−7020

Video S1. The scenario of chemical composition variation along the vacancy diffusion pathway is also observed in the direct MD simulations. A single vacancy diffusion event in the Cu−H system at 870 K and c_H = 0.1 is shown in the Supporting Information, Video S2, as an example. We can see from the animation that two H atoms are adsorbed near the vacancy center of the initial state before the vacancy jump. After two additional H atoms appear near the vacancy center of the final state accidentally, the vacancy diffusion occurs. When approaching the saddle state, one of the H atoms escapes from the vacancy center of the initial state. Thus, a total of three H atoms are adsorbed near the vacancy in the saddle-point state.

Here, we apply the Gibbs adsorption isotherm[34] in the H-vacancy system to illuminate the relationship between the H-enhanced vacancy diffusivity and the chemical composition excess in H at the initial and the saddle-point states. Following the Gibbsian concept, integrating eq 2 at constant P and T gives $\Delta G^m = -\int_{-\infty}^{\mu_H}\Gamma_H^m d\mu_H = -\int_{-\infty}^{\mu_H}(\Gamma_H^* - \Gamma_H^0)d\mu_H$, where the chemical potential of H at $-\infty$ corresponds to pure metals with $\Gamma_H^* = \Gamma_H^0 = 0$. Based on TST and a mean field approximation in lattice gas models[35] (see Sec. S7 in the Supporting Information), the vacancy diffusion coefficient ratio can be written as $D_{MH}^V/D_M^V = \exp(-\Delta G^m/k_BT)$ and

$$\Delta G^m = -\Gamma_{sat}^*\left[W\left(\frac{\Gamma_H^*}{\Gamma_{sat}^*}\right)^2 + k_BT\ln\frac{\Gamma_{sat}^*}{(\Gamma_{sat}^* - \Gamma_H^*)}\right] + \Gamma_{sat}^0\left[W\left(\frac{\Gamma_H^0}{\Gamma_{sat}^0}\right)^2 + k_BT\ln\frac{\Gamma_{sat}^0}{(\Gamma_{sat}^0 - \Gamma_H^0)}\right] \quad (3)$$

where W is an effective H−H interaction parameter, and Γ_{sat}^0 and Γ_{sat}^* are, respectively, the saturation values of Γ_H^0 and Γ_H^*. The values of W, Γ_{sat}^0, and Γ_{sat}^* can be determined by fitting the measured values of Γ_H^0, Γ_H^*, and ΔG^m in the PMF calculations. These fitted results gives a comparable result of D_{MH}^V/D_M^V with those from PMF, as shown in Figure 2(a,b). When $\mu_H \gg \overline{\mu}_H^0$ and $\mu_H \gg \overline{\mu}_H^*$, where $\overline{\mu}_H^0$ and $\overline{\mu}_H^*$ are, respectively, the standard values of the chemical potential at the ground and the saddle-point states, $d(\Delta G^m)/d\mu_H = -\Gamma_H^m \to -(\Gamma_{sat}^* - \Gamma_{sat}^0)$, which means that ΔG^m decreases linearly with increasing μ_H. Thus, $\Delta G^m \approx -(\Gamma_{sat}^* - \Gamma_{sat}^0)\Delta\mu_H$ and an activation excess, $\Gamma_H^m = \Gamma_{sat}^* - \Gamma_{sat}^0$, can be defined to characterize the "hydrogen lubrication" effect at high μ_H. The values of Γ_H^m are estimated to be 1.2 and 1.1 for Cu and Pd, respectively, based on the EAM potentials. Compared to the values of Γ_H^m at high H-concentrations using the *ab initio* GCMC (Figure 3(d)), we can approximately determine the $\Gamma_H^m \approx 1$ H at high μ_H for Cu and Pd.

We further demonstrated that the strong dragging effect of H on the vacancy diffusion given by the previous DFT calculations[17,18] can be avoided using the Cu−H system as an example through introducing the chemical composition variation of H along the diffusion pathway. At 0 K, the vacancy adsorbs H atoms from the H-environments as much as possible given that the Gibbs free-energy decreases (see Sec. S8 in the Supporting Information). Figure 4 shows the Gibbs free-energy along the diffusion pathway of a few H−vacancies complex in Cu computed from DFT using the Gibbs free-energy of a vacancy in pure Cu as a reference value. From Figure 4, we can see that the energy barrier for a vacancy without H (V_{H_0}) is about 0.72 eV. After minimization of the Gibbs free-energy of the vacancy, six H atoms occupy all the

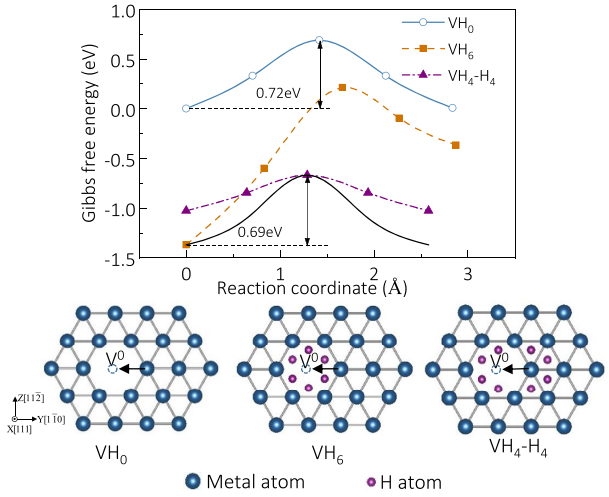

Figure 4. Gibbs free-energy as a function of reaction coordinate of the vacancy complex diffusion in Cu at 0 K computed using DFT. The below insets show the configurations of the fixed H-position, and the arrows show the jump direction of one Cu atom. The black line indicates the diffusion pathway considering the chemical composition variation of H along the vacancy diffusion pathway.

2NN(O) sites near the vacancy. When we fix the distribution of H over the diffusion process (VH_6), the energy barrier is as high as 1.58 eV. In contrast, the energy barrier can decrease to 0.69 eV only if the saddle state evolves to the atomic configurations that eight H atoms are adsorbed near the vacancy of both the initial and the final states (VH_4−H_4) to minimize the Gibbs free energy. Notably, although the chemical composition variation is demonstrated using the initial and the saddle states, the composition variation along the diffusion pathway is continuous (as qualitatively indicated by the black line in Figure 4).

The "hydrogen lubrication" effect on vacancy becomes more significant in higher H-concentration environments (e.g., c_H > 0.01, see Figure 2(a,b)). The H-concentration in metals ($c_H \equiv [H]/[M]$) can reach as high as 0.1∼1.0 in the high H_2 pressure and high temperature experiments, e.g., Pd, Ni, and Co with an FCC structure at P_{H_2} = 2.4−7.4 GPa and T = 930−1350 K.[36] However, the vacancy concentration ($c_V \equiv [V]/[M]$) in metals can be also as high as 0.1 through forming superabundant vacancies,[37] so whether there are still a sufficient number of H atoms that can be adsorbed by individual vacancies under experimental conditions needed to be considered. In the Pd−H system, c_V is very small for c_H < 0.6 and increases linearly with increasing c_H until c_V = 0.12 at c_H = 1 based on lattice contraction measurements, and c_H/c_V > 8.3 in the whole c_H range.[36] In the Nb−H system, c_H/c_V was found to be about 78 for c_H < 0.5 by electric resistivity measurement.[38] Since the maximum number of H atoms trapped in vacancy[39,40] is about 6, and the $\Gamma_H^m \approx 1$ H, every vacancy in the Pd−H and the Nb−H systems can easily access sufficient H atoms so that "hydrogen lubrication" can take effect. In the Ni−H, Co−H, and Fe−H systems, c_H/c_V were found to be 2.4, 2.6, and 3.4, respectively, for c_H < 0.8 through measuring the lattice contraction.[36,41] Thus, we expect there is sufficient hydrogen to drive the "hydrogen lubrication" effect under many experimental circumstances.

The activation excess caused by the chemical composition variation along the transition pathway should also affect the

https://dx.doi.org/10.1021/acs.jpclett.0c01798
J. Phys. Chem. Lett. 2020, 11, 7015−7020

kinetics of other defect motion under the H-environment, such as dislocation sliding by kink migration, grain boundary migration, and crack propagation, which also have higher capacity for attracting H due to positive activation volume (excess free volume) at the migration saddle-point. In addition to the above-mentioned classical mechanics treatment of H atoms, the quantum-dynamics effect of H[42] should be considered to determine the distribution of H along the vacancy diffusion pathway at an extremely low temperature, which is beyond the scope of this paper.

In conclusion, the present work addresses the effect of H on the vacancy diffusivity in FCC metals. We find that H atoms can enhance the diffusivity of vacancy due to a chemical composition variation along the vacancy diffusion pathway. An additional activation parameter beyond the well-known activation volume and activation entropy, the activation excess, is derived and can be used to characterize the migration frequency of lattice defects embedded in H-environments. If the activation excess Γ_H^m = 1 H, for every 10× increase in equivalent hydrogen gas partial pressure (fugacity) P_{H_2}, we would predict a 3.162× increase in vacancy mobility, regardless of temperature. We term such hydrogen-dependent defect mobility the "hydrogen lubrication" effect. The concept of a hydrogen Gibbs excess on the saddle state can be applied to other interstitial or substitutional solutes and to the other thermally activated processes of materials in environments containing O, He, N, C, and so on. This triplet of thermodynamic quantities, the Gibbsian activation excess, along with the more well-known activation volume and activation entropy (Meyer–Neldel compensation rule) form the complete characterization of mobile defects and shed light on the fundamental kinetics of defects of materials in service in complex chemical environments.

■ ASSOCIATED CONTENT

Supporting Information

The Supporting Information is available free of charge at https://pubs.acs.org/doi/10.1021/acs.jpclett.0c01798.

Supporting video captions, relationship between the vacancy mobility and the hydrogen Gibbs excess, computational details of free-energy barrier calculations based on the potential-of-mean-force method, absorbed H atoms at initial and saddle states, *ab initio* grand canonical Monte Carlo simulations, molecular dynamics simulations, mean field approximation in lattice gas model, Gibbs free energy using DFT at 0 K for Cu–H, construction of the EAM potential for Cu–H (PDF)

Video S1: Vacancy diffusion in Cu with c_H = 0.005 (left) and c_H = 0.1 (right) at 870 K for 10 ns using MD simulations (MP4)

Video S2: The H–vacancy complex diffusion in Cu at 870 K and c_H = 0.1 from MD simulations (MP4)

■ AUTHOR INFORMATION

Corresponding Authors

Ju Li – *Department of Nuclear Science and Engineering and Department of Materials Science and Engineering, Massachusetts Institute of Technology, Cambridge, Massachusetts 02139, United States;* orcid.org/0000-0002-7841-8058; Email: liju@mit.edu

Shigenobu Ogata – *Department of Mechanical Science and Bioengineering, Osaka University, Osaka 560-8531, Japan; Center for Elements Strategy Initiative for Structural Materials, Kyoto University, Kyoto 606-8501, Japan;* Email: ogata@me.es.osaka-u.ac.jp

Authors

Jun-Ping Du – *Center for Elements Strategy Initiative for Structural Materials, Kyoto University, Kyoto 606-8501, Japan; Department of Mechanical Science and Bioengineering, Osaka University, Osaka 560-8531, Japan*

W. T. Geng – *Department of Mechanical Science and Bioengineering, Osaka University, Osaka 560-8531, Japan; University of Science and Technology Beijing, Beijing 100083, China;* orcid.org/0000-0002-9838-5644

Kazuto Arakawa – *Next Generation TATARA Co-Creation Centre, Organization for Industrial Innovation, Shimane University, Matsue 690-8504, Japan*

Complete contact information is available at: https://pubs.acs.org/10.1021/acs.jpclett.0c01798

Notes

The authors declare no competing financial interest.

■ ACKNOWLEDGMENTS

This work was supported by the Element Strategy Initiative for Structural Materials (ESISM) of MEXT, Grant Number JPMXP0112101000. Part of the calculations were performed on the large-scale computer systems at the Cybermedia Center, Osaka University. S.O. acknowledges the support by the JSPS KAKENHI Grant Nos. JP18H05450, JP18H05453, JP17H01238, and JP17K18827. W.T.G. thanks the NSFC (Grant Number U1760203) for support. J.L. acknowledges support by the U.S. Department of Energy (DOE) Fuel Cell Technologies Office under award number DE-EE0008830.

■ REFERENCES

(1) Pundt, A.; Kirchheim, R. Hydrogen in Metals: Microstructural Aspects. *Annu. Rev. Mater. Res.* **2006**, *36*, 555–608.

(2) Jeon, K.-J.; Moon, H. R.; Ruminski, A. M.; Jiang, B.; Kisielowski, C.; Bardhan, R.; Urban, J. J. Air-Stable Magnesium Nanocomposites Provide Rapid and High-Capacity Hydrogen Storage without Using Heavy-Metal Catalysts. *Nat. Mater.* **2011**, *10*, 286–290.

(3) Yoon, H.; Choi, M.; Lim, T.-W.; Kwon, H.; Ihm, K.; Kim, J. K.; Choi, S.-Y.; Son, J. Reversible Phase Modulation and Hydrogen Storage in Multivalent VO_2 Epitaxial Thin Films. *Nat. Mater.* **2016**, *15*, 1113–1119.

(4) Christofides, C.; Mandelis, A. Solid-state Sensors for Trace Hydrogen Gas Detection. *J. Appl. Phys.* **1990**, *68*, R1–R30.

(5) Schmid, G. Large Clusters and Colloids. Metals in the Embryonic State. *Chem. Rev.* **1992**, *92*, 1709–1727.

(6) Sen, P.; Alam, K.; Das, T.; Banerjee, R.; Chakraborty, S. Combinatorial Design and Computational Screening of Two-Dimensional Transition Metal Trichalcogenide Monolayers: Toward Efficient Catalysts for Hydrogen Evolution Reaction. *J. Phys. Chem. Lett.* **2020**, *11*, 3192–3197.

(7) Troiano, A. R. The Role of Hydrogen and Other Interstitials in the Mechanical Behavior of Metals. *Metallogr., Microstruct., Anal.* **2016**, *5*, 557–569.

(8) Nagumo, M. Hydrogen Related Failure of Steels – a New Aspect. *Mater. Sci. Technol.* **2004**, *20*, 940–950.

(9) Neeraj, T.; Srinivasan, R.; Li, J. Hydrogen Embrittlement of Ferritic Steels: Observations on Deformation Microstructure, Nanoscale Dimples and Failure by Nanovoiding. *Acta Mater.* **2012**, *60*, 5160–5171.

(10) Xie, D.-G.; Wang, Z.-J.; Sun, J.; Li, J.; Ma, E.; Shan, Z.-W. In Situ Study of the Initiation of Hydrogen Bubbles at the Aluminium Metal/Oxide Interface. *Nat. Mater.* **2015**, *14*, 899−903.
(11) Geng, W. T.; Wan, L.; Du, J.-P.; Ishii, A.; Ishikawa, N.; Kimizuka, H.; Ogata, S. Hydrogen Bubble Nucleation in α-Iron. *Scr. Mater.* **2017**, *134*, 105−109.
(12) Hou, J.; Kong, X.-S.; Wu, X.; Song, J.; Liu, C. S. Predictive Model of Hydrogen Trapping and Bubbling in Nanovoids in Bcc Metals. *Nat. Mater.* **2019**, *18*, 833−839.
(13) Hänggi, P.; Talkner, P.; Borkovec, M. Reaction-Rate Theory: Fifty Years after Kramers. *Rev. Mod. Phys.* **1990**, *62*, 251−341.
(14) Kirkendall, E. O. Diffusion of Zinc in Alpha Brass. *Trans. Metall. Soc. AIME* **1942**, *147*, 104−110.
(15) Smigelskas, A. D.; Kirkendall, E. O. Zinc Diffusion in Alpha Brass. *Trans. Metall. Soc. AIME* **1947**, *171*, 130−142.
(16) Myers, S. M.; Baskes, M. I.; Birnbaum, H. K.; Corbett, J. W.; Deleo, G. G.; Estreicher, S. K.; Haller, E. E.; Jena, P.; Johnson, N. M.; Kirchheim, R.; Pearton, S. J.; Stavola, M. J. Hydrogen Interactions with Defects in Crystalline Solids. *Rev. Mod. Phys.* **1992**, *64*, 559−617.
(17) Wang, Y.; Connétable, D.; Tanguy, D. Hydrogen Influence on Diffusion in Nickel from First-Principles Calculations. *Phys. Rev. B: Condens. Matter Mater. Phys.* **2015**, *91*, No. 094106.
(18) Hayward, E.; Fu, C. C. Interplay between Hydrogen and Vacancies in α-Fe. *Phys. Rev. B: Condens. Matter Mater. Phys.* **2013**, *87*, 174103.
(19) Kirchheim, R. Reducing Grain Boundary, Dislocation Line and Vacancy Formation Energies by Solute Segregation. I. Theoretical Background. *Acta Mater.* **2007**, *55*, 5129−5138.
(20) Kirchheim, R. Reducing Grain Boundary, Dislocation Line and Vacancy Formation Energies by Solute Segregation: II. Experimental Evidence and Consequences. *Acta Mater.* **2007**, *55*, 5139−5148.
(21) Zhu, T.; Li, J. Ultra-Strength Materials. *Prog. Mater. Sci.* **2010**, *55*, 710−757.
(22) Hara, S.; Li, J. Adaptive Strain-Boost Hyperdynamics Simulations of Stress-Driven Atomic Processes. *Phys. Rev. B: Condens. Matter Mater. Phys.* **2010**, *82*, 184114.
(23) Li, Q.-J.; Xu, B.; Hara, S.; Li, J.; Ma, E. Sample-Size-Dependent Surface Dislocation Nucleation in Nanoscale Crystals. *Acta Mater.* **2018**, *145*, 19−29.
(24) Den Otter, W. K.; Briels, W. J. Free Energy from Molecular Dynamics with Multiple Constraints. *Mol. Phys.* **2000**, *98*, 773−781.
(25) Sugimoto, H.; Fukai, Y. Solubility of Hydrogen in Metals under High Hydrogen Pressures: Thermodynamical Calculations. *Acta Metall. Mater.* **1992**, *40*, 2327−2336.
(26) Fukai, Y. Hydrogen-Induced Superabundant Vacancies in Metals: Implication for Electrodeposition. *Defect Diffus. Forum* **2011**, *312*−*315*, 1106−1115.
(27) Baranowski, B.; Majchrzak, S.; Flanagan, T. B. The Volume Increase of Fcc Metals and Alloys Due to Interstitial Hydrogen over a Wide Range of Hydrogen Contents. *J. Phys. F: Met. Phys.* **1971**, *1*, 258−261.
(28) Fukumuro, N.; Yokota, M.; Yae, S.; Matsuda, H.; Fukai, Y. Hydrogen-Induced Enhancement of Atomic Diffusion in Electrodeposited Pd Films. *J. Alloys Compd.* **2013**, *580*, S55−S57.
(29) Mishin, Y.; Mehl, M. J.; Papaconstantopoulos, D. A.; Voter, A. F.; Kress, J. D. Structural Stability and Lattice Defects in Copper: Ab Initio, Tight-Binding, and Embedded-Atom Calculations. *Phys. Rev. B: Condens. Matter Mater. Phys.* **2001**, *63*, 224106.
(30) Du, J. P.; Wang, C. Y.; Yu, T. Construction and Application of Multi-Element EAM Potential (Ni-Al-Re) in γ/γ′ Ni-Based Single Crystal Superalloys. *Modell. Simul. Mater. Sci. Eng.* **2013**, *21*, No. 015007.
(31) Zhou, X. W.; Zimmerman, J. A.; Wong, B. M.; Hoyt, J. J. An Embedded-Atom Method Interatomic Potential for Pd−H Alloys. *J. Mater. Res.* **2008**, *23*, 704−718.
(32) Mehrer, H. *Diffusion in Solids: Fundamentals, Methods, Materials, Diffusion-Controlled Processes*; Springer: Berlin, 2007.
(33) Wexler, R. B.; Qiu, T.; Rappe, A. M. Automatic Prediction of Surface Phase Diagrams Using Ab Initio Grand Canonical Monte Carlo. *J. Phys. Chem. C* **2019**, *123*, 2321−2328.
(34) Chattoraj, D. K.; Birdi, K. S. *Adsorption and the Gibbs Surface Excess*; Plenum: New York, 1984.
(35) Kirchheim, R.; Somerday, B.; Sofronis, P. Chemomechanical Effects on the Separation of Interfaces Occurring during Fracture with Emphasis on the Hydrogen-Iron and Hydrogen-Nickel System. *Acta Mater.* **2015**, *99*, 87−98.
(36) Harada, S.; Yokota, S.; Ishii, Y.; Shizuku, Y.; Kanazawa, M.; Fukai, Y. A Relation between the Vacancy Concentration and Hydrogen Concentration in the Ni−H, Co−H and Pd−H Systems. *J. Alloys Compd.* **2005**, *404*−*406*, 247−251.
(37) Fukai, Y.; Ōkuma, N. Formation of Superabundant Vacancies in Pd Hydride under High Hydrogen Pressures. *Phys. Rev. Lett.* **1994**, *73*, 1640−1643.
(38) Koike, H.; Shizuku, Y.; Yazaki, A.; Fukai, Y. Superabundant Vacancy Formation in Nb−H Alloys; Resistometric Studies. *J. Phys.: Condens. Matter* **2004**, *16*, 1335−1349.
(39) Fukai, Y. Hydrogen-Induced Enhancement of Atomic Diffusion in Metals. *Defect Diffus. Forum* **2010**, *297*−*301*, 132−141.
(40) Nazarov, R.; Hickel, T.; Neugebauer, J. Ab Initio Study of H-Vacancy Interactions in Fcc Metals: Implications for the Formation of Superabundant Vacancies. *Phys. Rev. B: Condens. Matter Mater. Phys.* **2014**, *89*, 144108.
(41) Hiroi, T.; Fukai, Y.; Mori, K. The Phase Diagram and Superabundant Vacancy Formation in Fe−H Alloys Revisited. *J. Alloys Compd.* **2005**, *404*−*406*, 252−255.
(42) Kimizuka, H.; Ogata, S.; Shiga, M. Unraveling Anomalous Isotope Effect on Hydrogen Diffusivities in Fcc Metals from First Principles Including Nuclear Quantum Effects. *Phys. Rev. B: Condens. Matter Mater. Phys.* **2019**, *100*, No. 024104.

https://dx.doi.org/10.1021/acs.jpclett.0c01798
J. Phys. Chem. Lett. 2020, 11, 7015−7020

Hydrogen-Enhanced Vacancy Diffusion in Metals

Jun-Ping Du[1,2], W. T. Geng[2,3], Kazuto Arakawa[4], Ju Li[5] and Shigenobu Ogata[2,1†]*

[1] Center for Elements Strategy Initiative for Structural Materials, Kyoto University, Kyoto 606-8501, Japan.

[2] Department of Mechanical Science and Bioengineering, Osaka University, Osaka 560-8531, Japan.

[3] University of Science and Technology Beijing, Beijing 100083, China.

[4] Next Generation TATARA Co-Creation Centre, Organization for Industrial Innovation, Shimane University, 1060 Nishikawatsu, Matsue 690-8504, Japan.

[5] Department of Nuclear Science and Engineering and Department of Materials Science and Engineering, Massachusetts Institute of Technology, Cambridge, MA, 02139, USA.

Corresponding Author

* Corresponding author. liju@mit.edu

† Corresponding author. ogata@me.es.osaka-u.ac.jp

This PDF file includes:

S1. Supporting video caption

Video S1:"Vacancy_diffusion.mp4". Vacancy diffusion in Cu with c_H = 0.005 (Left) and c_H = 0.1 (Right) at 870 K for 10 ns using MD simulations. The navy balls are the Cu atoms involved in the Cu-vacancy exchanges with a displacement larger than 1.5 Å using the configuration at timestep = 0 as a reference state. The orange arrows are the displacement vector of the Cu atoms. Thus, trajectory of the vacancy can be indicated by the arrows. The other Cu atoms and H atoms are not shown.

Video S2: "VHn_diffusion_Cu.mp4". The H–vacancy complex diffusion in Cu at 870 K and c_H = 0.1 from MD simulations. The big navy balls are Cu atoms; the big pink ball is the jumping Cu; the small white balls are H atoms; the small green balls are the adsorbed H atoms at the initial state; the small red balls are the additionally adsorbed H atoms at the saddle state.

S2. Relationship between the vacancy mobility and the hydrogen Gibbs excess

The chemical potential of H atoms (μ_H) is defined as one-half of the chemical potential of H_2 gas (μ_{H_2}), and thus related to the fugacity (f) of H_2 gas by $2\mu_H = \mu_{H_2} = \mu^0_{H_2} + k_B T \ln f$, where $\mu^0_{H_2}$ is the standard value and is a function of temperature. At a fixed temperature and constant hydrogen Gibbs excess (Γ^m_H), the Gibbs free energy barrier decrease due to 10 times increase in the fugacity is $\Delta G^m = -\int_{f_1}^{f_2} \Gamma^m_H d\left(\frac{1}{2}\mu_{H_2}\right) = -\int_{f_1}^{f_2} \Gamma^m_H d\left(\frac{1}{2}\mu^0_{H_2} + \frac{1}{2}k_B T \ln f\right) = -k_B T \Gamma^m_H \ln\sqrt{\frac{f_2}{f_1}}$, where $\frac{f_2}{f_1} = 10$. When $\Gamma^m_H = 1$, the mobility increase by a ($\exp(-\Delta G^m / k_B T) = (f_2 / f_1)^{1/2} \approx$) 3.162-fold. We can see that the absolute value of ΔG^m itself decreases with decreasing temperature under the expedient assumption of the constant hydrogen Gibbs excess (Γ^m_H =1), although the mobility increase is temperature independent. However, practically Γ^m_H is temperature-dependent, and should not be exactly one.

S3. Free-energy barrier calculations based on the potential-of-mean-force (PMF) method

The free-energy barrier of the vacancy diffusion along the prescribed reaction coordinate were computed using the PMF method[1] with a hybrid constrained-MD/GCMC simulation for the Cu–H and Pd–H system at 870 K. The interatomic interaction of the Cu–H and Pd–H systems are

suitable to be described by the EAM potentials.[2–4] The EAM potential of Cu developed by Mishin et al.[5] was adopted for the Cu–Cu potential, and the H–H potential and the Cu–H cross-potential were developed on the basis of the forms of the potentials reported by Du et al.[6] (see Sce. S9 in Supporting Information). The EAM potential of Pd–H developed by Zhou et al.[7] was adopted for the Pd–H system. The size of the simulation model was $(10 \times 10 \times 10)a_0$, where a_0 is the lattice constant of Cu or Pd obtained by the EAM. The periodic boundary conditions were imposed in all three directions and a single vacancy was created in the model by removing a metal atom. The H-atoms were inserted/deleted using the GCMC method with the fixed chemical potential of H-atoms. The reaction coordinate was chosen as the relative displacement vector between one of the metals atoms surrounding the vacancy and the center of mass of the remanding metal atoms. A small spherical repulsive wall was set at the center of the vacancy to rebound back only the metal atoms that spontaneously jump into the vacancy so that we could successfully sample the configuration of the H-vacancy complexes. The atomic structure with the prescribed value of reaction coordinate was given by the metal–vacancy exchange in pure metals using the nudged elastic band (NEB) method.[8] Based on the constrained-MD method,[9] the prescribed value of the reaction coordinate, the model size and the temperature were fixed in the simulations. The H-atoms were inserted/deleted using the GCMC method with the fixed chemical potential of H-atoms. The average pressure in the metal–H systems is almost 0 Pa by adjusting the model size carefully. The free-energy barrier can be given by the integral of the time-averaged force on the metal atom over the reaction coordinates of the vacancy diffusion from the initial energy minimum to the saddle state.

S4. Absorbed H-atoms at initial and saddle states

The ability to adsorb H of these interstitial sites can be qualitatively characterized by the segregation energy, which is the energy needed to move a single H-atom from the bulk metals to these sites. According to the result of the segregation energy (see Figures S7 and S8), the H-atoms within the 2NN interstitial sites are strongly bounded at the initial state of vacancy diffusion. At the saddle state of the vacancy diffusion, not only the abovementioned sites near the vacancy center at the initial state, but also the interstitial sites within the 2NN of the vacancy center at the final state can also adsorb H-atoms. To eliminate the disturbance of thermal vibration, the energy of the systems are minimized under the same constraints used in the constrained-MD simulations. The H-atoms at those interstitial sites are then counted as being adsorbed. The average value of the adsorbed H-atoms and the corresponding standard error are obtained using 2000 configurations taken from the constrained-MD simulations.

S5. *Ab initio* grand canonical Monte Carlo simulations

We carried out the *ab initio* GCMC simulations using the LAMMPS[10] code and the VASP code.[11–13] The LAMMPS as a "client" code performs the GCMC simulation and communicates with the "server" code, VASP, when the energy of system based on DFT is required. The electron–ion interaction in the DFT was described using the projector-augmented wave method.[14] The exchange correlation between electrons was treated with the generalized gradient approximation in the Perdew–Burke–Ernzerhof form[15] and the energy cutoff was 360 eV for the plane-wave basis set. The average bulk H-concentration and the adsorbed H in vacancy diffusion process were determined using the *ab initio* GCMC simulations with a $(1 \times 1 \times 1)a_0$ FCC lattice and a $(2 \times 2 \times 2)a_0$ FCC lattice with one vacancy, respectively, under a specific chemical potential of H-

atoms and a constant temperature of 870 K, where a_0 is the lattice constant of Cu or Pd obtained by DFT. The NEB method[8] was employed to give the saddle-state configuration of vacancy–metal exchange based on DFT. In the NEB calculations, atomic positions were relaxed until the atomic forces were smaller than 0.02 eV/Å. All metal atoms were fixed in the *ab initio* GCMC simulations, while the H-atoms were moved and inserted/deleted in the "internal surface" of the initial- and the saddle-state of vacancy diffusion. The "internal surface" of vacancy is defined by the spherical regions at vacancy centers with a radii of $(\sqrt{2}/2+1/2)a_0/2$, which encompasses the 1NN and the 2NN interstitial sites of the vacancy. The translation and the insertion operations are skipped if any atom pairs are closer than 0.8 Å, because such close distances lead to a very high energy and the operations are always rejected by GCMC.

We evaluated the effect of thermal expansion of lattice and the thermal movement of metals atom in Pd–H system on the hydrogen Gibbs excess in the *ab initio* GCMC simulations to ensure the two effects can be safely ignored in the simulations. To include thermal expansion of metal lattice, the experimental thermal expansion coefficient of lattice[16] at 870 K of pure metals Pd were adopted in these calculations. Under the expanded lattice, the four metal atoms in the $(1 \times 1 \times 1)a_0$ FCC lattice and the first-nearest-neighboring metal atoms of vacancy in the a $(2 \times 2 \times 2)a_0$ FCC lattice (12 metal atoms around the V^0 in the initial state in Figure 1, and 18 metal atoms around both the V^0 and the V^1 in the saddle-point state, but except for the metal atom located at the saddle-point) were allowed to move using the MC method at 870 K. The results of adsorbed H are shown in Figure S1. We can see that the number adsorbed H is almost consistent with the simulations without considering thermal expansion and thermal movement of metal atoms. Thus, the approximations do not change our conclusions that there is Gibbs excess of H on the saddle point configuration of vacancy migration.

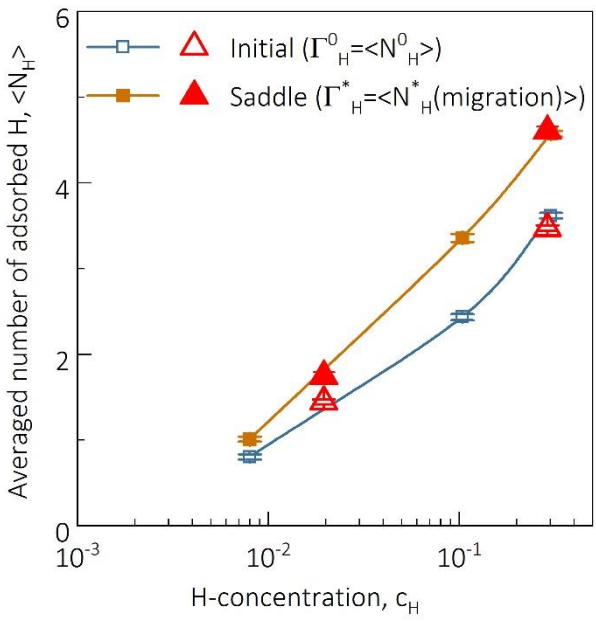

Figure S1. The number of adsorbed H-atoms in the initial and the saddle states of the vacancy diffusion in Pd–H systems by considering the thermal expansion of lattice and thermal movement of metal atoms (Filled and open triangles symbols), in comparison with those ignoring the two effects in the simulations (Filled and open square symbols).

The setting of the *ab initio* GCMC simulations are as follows. In each *ab initio* GCMC step, every metal atoms was attempted to move once in average using the MC method if the metal atom was allowed to move. For the H-atoms, four displacement operations and two insertion/deletion operations were performed in the initial state, while eight displacement operations and four insertion/deletion operations were performed in the saddle state in each *ab initio* GCMC step. We firstly performed one *ab initio* GCMC simulations with 100 GCMC steps. Then, six configurations with different numbers of H-atom appeared in the first GCMC simulations were randomly chosen as the input configuration to perform six subsequent *ab initio* GCMC simulations with 70-100 GCMC steps. All the configurations (400-600 configurations) given by the subsequent *ab-initio*

GCMC simulations were used to calculate the average value of adsorbed H-atoms and the corresponding standard error.

S6. Molecular dynamics simulations

We carried out the MD simulation using the LAMMPS[10] code with the EAM potentials used in the PMF simulations (Sec. S3). The size of the MD model of vacancy diffusion was $(10 \times 10 \times 10)a_0$, where a_0 is the lattice constant of Cu or Pd obtained by EAM. A single vacancy was created in the model by removing a metal atom. The H-atoms were randomly distributed in the system, and the periodic boundary conditions were imposed in all three directions. The simulation was conducted under an isobaric–isothermal ensemble for 10 ns. The external pressure (P) was 0 Pa at a temperature of 870 K, and the time step was set to 1 fs. The temperature of 870 K was selected so that vacancy diffusion could be observed frequently (>10 jumps/ns) even at the MD timescale. The mean squared displacement (MSD) of all metal-atoms $< R^2 >_{\mathrm{M}}$ in the MD model with a single vacancy was estimated, which is related to the diffusion coefficient of metal atoms, D^{M}, through the Einstein–Smoluchowski relation[17]: $D^{\mathrm{M}} =< R^2 >_{\mathrm{M}} /(6t)$. The diffusion of metal atoms is achieved via metal–vacancy exchange. The number of vacancies is almost fixed as one in the MD timescale, and the diffusion of vacancies is uncorrelated; therefore, the MSD of Cu-atoms can be related to the MSD of the vacancies, $< R^2 >_{\mathrm{V}}$, by $< R^2 >_{\mathrm{V}} = N < R^2 >_{\mathrm{M}} / f$, where N is the number of metal-atoms and $f = 0.781$ is the correlation factor.[17] Thus, the vacancy diffusion coefficient D^{V} is given by $D^{\mathrm{V}} =< R^2 >_{\mathrm{V}} /(6t) = ND^{\mathrm{M}} / f$. Forty samples of MD simulations for the pure metals and fifteen samples for the metal–H systems with different initial H positions and different atomic velocities were used to calculate the average diffusion coefficient.

S7. Mean field approximation in lattice gas model

Based on a mean field approximation in lattice gas models,[18] the chemical potential of H-atoms in metals can be approximate by

$$\begin{aligned}\mu_{\mathrm{H}} &= \bar{\mu}_{\mathrm{H}}^{0} + 2W\frac{\Gamma_{\mathrm{H}}^{0}}{\Gamma_{\mathrm{sat}}^{0}} + k_B T \ln\frac{\Gamma_{\mathrm{H}}^{0}}{\Gamma_{\mathrm{sat}}^{0}-\Gamma_{\mathrm{H}}^{0}} \\ &= \bar{\mu}_{\mathrm{H}}^{*} + 2W\frac{\Gamma_{\mathrm{H}}^{*}}{\Gamma_{\mathrm{sat}}^{*}} + k_B T \ln\frac{\Gamma_{\mathrm{H}}^{*}}{\Gamma_{\mathrm{sat}}^{*}-\Gamma_{\mathrm{H}}^{*}}\end{aligned}, \qquad \textbf{(S1)}$$

where $\bar{\mu}_{\mathrm{H}}^{0}$ and $\bar{\mu}_{\mathrm{H}}^{*}$ are, respectively, the standard values of the chemical potential at the ground and the saddle-point states, W is an effective H-H interaction parameter, and $\Gamma_{\mathrm{sat}}^{0}$ and $\Gamma_{\mathrm{sat}}^{*}$ are, respectively, the saturation value of Γ_{H}^{0} and Γ_{H}^{*}. Using Eq. (S1), the vacancy diffusion coefficient ratio with and without H in metals, $D_{\mathrm{MH}}^{\mathrm{V}} / D_{\mathrm{M}}^{\mathrm{V}}$, can be written as (M = Cu or Pd)

$$\begin{aligned}\frac{D_{\mathrm{MH}}^{\mathrm{V}}}{D_{\mathrm{M}}^{\mathrm{V}}} &= \exp\left(-\frac{\Delta G^{\mathrm{m}}}{k_{\mathrm{B}}T}\right) = \left(\frac{\Gamma_{\mathrm{sat}}^{*}}{\Gamma_{\mathrm{sat}}^{*}-\Gamma_{\mathrm{H}}^{*}}\right)^{\Gamma_{\mathrm{sat}}^{*}}\left(\frac{\Gamma_{\mathrm{sat}}^{0}-\Gamma_{\mathrm{H}}^{0}}{\Gamma_{\mathrm{sat}}^{0}}\right)^{\Gamma_{sat}^{0}} \\ &\times\exp\left\{\frac{W}{k_{\mathrm{B}}T}\left[\Gamma_{\mathrm{sat}}^{*}\left(\frac{\Gamma_{\mathrm{H}}^{*}}{\Gamma_{\mathrm{sat}}^{*}}\right)^{2} - \Gamma_{sat}^{0}\left(\frac{\Gamma_{\mathrm{H}}^{0}}{\Gamma_{\mathrm{sat}}^{0}}\right)^{2}\right]\right\}\end{aligned}. \qquad \textbf{(S2)}$$

The values of $\bar{\mu}_{\mathrm{H}}^{0}$, $\bar{\mu}_{\mathrm{H}}^{*}$, $\Gamma_{\mathrm{sat}}^{0}$, $\Gamma_{\mathrm{sat}}^{*}$ and W can be determined by fitting the Eqs. (S1) and (S2) using the measured value of Γ_{H}^{0}, Γ_{H}^{*}, and $D_{\mathrm{MH}}^{\mathrm{V}} / D_{\mathrm{M}}^{\mathrm{V}}$ in the PMF calculations and the corresponding chemical potential of H-atoms. For Cu–H system, we get $\bar{\mu}_{\mathrm{H}}^{0} = -0.80$ eV, $\bar{\mu}_{\mathrm{H}}^{*} = -0.81$ eV, $\Gamma_{\mathrm{sat}}^{0} = 6.07$, $\Gamma_{\mathrm{sat}}^{*} = 7.26$ and $W = 0.07$ eV. For Pb–H system, we get $\bar{\mu}_{\mathrm{H}}^{0} = -2.42$ eV, $\bar{\mu}_{\mathrm{H}}^{*} = -2.46$ eV, $\Gamma_{\mathrm{sat}}^{0} = 5.71$, $\Gamma_{\mathrm{sat}}^{*} = 6.81$ and $W = 0.02$ eV.

S8. Gibbs free energy using DFT at 0 K for Cu–H

The NEB method[8] was employed to calculate the energy barriers of vacancy–Cu exchange based on DFT. Three images were linearly interpolated for each reaction pathway, resulting in a total of five images for each migration path. In the NEB calculations, atomic positions were relaxed until the atomic forces were smaller than 0.02 eV/Å. We have also checked the phonon frequency of saddle-point configuration to confirm that there is only one imaginary frequency which guarantees it is a saddle-point. The relative Gibbs free-energy of the H-vacancy system at 0 K is computed as $\Delta G = E\left(\mathrm{Cu}_{107}\mathrm{VH}_n\right) - n\mu_{\mathrm{H}} - E\left(\mathrm{Cu}_{107}\mathrm{VH}_0\right)$, where $E\left(\mathrm{Cu}_{107}\mathrm{VH}_n\right)$ is the energy of a $(3 \times 3 \times 3)a_0$ FCC Cu lattice with one Cu vacancy adsorbing n H-atoms and at a specific reaction coordinate, and a_0 = 3.63 Å is the Cu lattice constant computed using the DFT. $E\left(\mathrm{Cu}_{107}\mathrm{VH}_n\right) - n\mu_{\mathrm{H}}$ is the Gibbs free energy of the VH_n complex, and $E\left(\mathrm{Cu}_{107}\mathrm{VH}_0\right)$ is the energy of the reference state that is a $(3 \times 3 \times 3)a_0$ FCC Cu lattice with one vacancy. $\mu_{\mathrm{H}} = E\left(\mathrm{Cu}_{108}\mathrm{H}\right) - E\left(\mathrm{Cu}_{108}\right)$ is the chemical potential of H at 0 K, where $E\left(\mathrm{Cu}_{108}\right)$ and $E\left(\mathrm{Cu}_{108}\mathrm{H}\right)$ are the energies of the $(3 \times 3 \times 3)a_0$ FCC Cu lattice and that with a H-atom at 2NN(O) site, respectively. This definition of Gibbs free energy at 0K is consistent with the limit of Eq. (3) as the temperature approaches zero. We can derive the relationship between these two equations as follows. Using the Eq.(S1), We can write, $k_{\mathrm{B}}T = \dfrac{\mu_{\mathrm{H}} - \bar{\mu}^{*}_{\mathrm{H}} - 2W\dfrac{\Gamma^{*}_{\mathrm{H}}}{\Gamma^{*}_{\mathrm{sat}}}}{\ln\dfrac{\Gamma^{*}_{\mathrm{H}}}{\Gamma^{*}_{\mathrm{sat}} - \Gamma^{*}_{\mathrm{H}}}} = \dfrac{\mu_{\mathrm{H}} - \bar{\mu}^{0}_{\mathrm{H}} - 2W\dfrac{\Gamma^{0}_{\mathrm{H}}}{\Gamma^{0}_{\mathrm{sat}}}}{\ln\dfrac{\Gamma^{0}_{\mathrm{H}}}{\Gamma^{0}_{\mathrm{sat}} - \Gamma^{0}_{\mathrm{H}}}}$. Inserting $k_{\mathrm{B}}T$ into Eq.(3), we get

$$\Delta G^{\mathrm{m}} = -\Gamma_{\mathrm{sat}}^{*}\left[W\left(\frac{\Gamma_{\mathrm{H}}^{*}}{\Gamma_{\mathrm{sat}}^{*}}\right)^{2} + \left(\mu_{\mathrm{H}} - \bar{\mu}_{\mathrm{H}}^{*} - 2W\frac{\Gamma_{\mathrm{H}}^{*}}{\Gamma_{\mathrm{sat}}^{*}}\right)\frac{\ln\dfrac{\Gamma_{\mathrm{sat}}^{*}}{\left(\Gamma_{\mathrm{sat}}^{*}-\Gamma_{\mathrm{H}}^{*}\right)}}{\ln\dfrac{\Gamma_{\mathrm{H}}^{*}}{\Gamma_{\mathrm{sat}}^{*}-\Gamma_{\mathrm{H}}^{*}}}\right]$$
$$+\Gamma_{\mathrm{sat}}^{0}\left[W\left(\frac{\Gamma_{\mathrm{H}}^{0}}{\Gamma_{\mathrm{sat}}^{0}}\right)^{2} + \left(\mu_{\mathrm{H}} - \bar{\mu}_{\mathrm{H}}^{0} - 2W\frac{\Gamma_{\mathrm{H}}^{0}}{\Gamma_{\mathrm{sat}}^{0}}\right)\frac{\ln\dfrac{\Gamma_{\mathrm{sat}}^{0}}{\left(\Gamma_{\mathrm{sat}}^{0}-\Gamma_{\mathrm{H}}^{0}\right)}}{\ln\dfrac{\Gamma_{\mathrm{H}}^{0}}{\Gamma_{\mathrm{sat}}^{0}-\Gamma_{\mathrm{H}}^{0}}}\right]\cdot$$

When the temperature approaches zero, the Γ_{H}^{0} and Γ_{H}^{*} approach their saturation value, $\Gamma_{\mathrm{sat}}^{0}$ and $\Gamma_{\mathrm{sat}}^{*}$, respectively. Then, ΔG^{m} at 0K can be write as,

$$\begin{aligned}\Delta G^{\mathrm{m}} &= -\Gamma_{\mathrm{sat}}^{*}(\mu_{\mathrm{H}} - \bar{\mu}_{\mathrm{H}}^{*} - W) + \Gamma_{\mathrm{sat}}^{0}(\mu_{\mathrm{H}} - \bar{\mu}_{\mathrm{H}}^{0} - W)\\ &= [\Gamma_{\mathrm{sat}}^{*}(\bar{\mu}_{\mathrm{H}}^{*} + W) - \Gamma_{\mathrm{sat}}^{*}\mu_{\mathrm{H}}] - [\Gamma_{\mathrm{sat}}^{0}(\bar{\mu}_{\mathrm{H}}^{0} + W) - \Gamma_{\mathrm{sat}}^{0}\mu_{\mathrm{H}}]\end{aligned}\cdot$$

The terms of $\Gamma_{\mathrm{sat}}^{*}(\bar{\mu}_{\mathrm{H}}^{*} + W)$ and $\Gamma_{\mathrm{sat}}^{0}(\bar{\mu}_{\mathrm{H}}^{0} + W)$ are the total energy changes of the saddle-point and the initial states induced by the H segregation, respectively, which can be directly included in the DFT total energy calculations. Using VH_6 at its initial state as an example, $\Gamma_{\mathrm{H}}^{0} = \Gamma_{\mathrm{sat}}^{0} = 6$; $\bar{\mu}_{\mathrm{H}}^{0} = E\left(\mathrm{Cu}_{107}\mathrm{VH}_1\right) - E\left(\mathrm{Cu}_{107}\mathrm{VH}_0\right)$ is standard value in DFT calculation and corresponds to the total energy change by introducing one H atom in the vacancy; the total H-H interaction energy of the VH_6 complex is

$$W\left.\frac{\left(\Gamma_{\mathrm{H}}^{0}\right)^{2}}{\Gamma_{\mathrm{sat}}^{0}}\right|_{\Gamma_{\mathrm{H}}^{0}=\Gamma_{\mathrm{sat}}^{0}} = \Gamma_{\mathrm{sat}}^{0}W = E\left(\mathrm{Cu}_{107}\mathrm{VH}_6\right) + 5E\left(\mathrm{Cu}_{107}\mathrm{VH}_0\right) - 6E\left(\mathrm{Cu}_{107}\mathrm{VH}_1\right),$$ which corresponds to the total energy change by transforming six VH_1 complex to one VH_6 complex and five empty vacancies. Then, inserting $\bar{\mu}_{\mathrm{H}}^{0}$ and $\Gamma_{\mathrm{sat}}^{0}W$ into $\Gamma_{\mathrm{sat}}^{0}(\bar{\mu}_{\mathrm{H}}^{0} + W)$, we can see that

$\Gamma_{\text{sat}}^{0}(\overline{\mu}_{\text{H}}^{0}+W)=E\left(\text{Cu}_{107}\text{VH}_6\right)-E\left(\text{Cu}_{107}\text{VH}_0\right)$ is the total energy change of a vacancy due to the segregation of six Hs. While $\Gamma_{\text{sat}}^{0}(\overline{\mu}_{\text{H}}^{0}+W)-\Gamma_{\text{sat}}^{0}\mu_{\text{H}}=\left[E\left(\text{Cu}_{107}\text{VH}_6\right)-\Gamma_{\text{sat}}^{0}\mu_{\text{H}}\right]-E\left(\text{Cu}_{107}\text{VH}_0\right)$ is the Gibbs free energy change due to segregation of six Hs. Thus, the Gibbs free energy of VH_6 is $E\left(\text{Cu}_{107}\text{VH}_6\right)-\Gamma_{\text{sat}}^{0}\mu_{\text{H}}$. So, the definition of the Gibbs free energy of VH_n as $E\left(\text{Cu}_{107}\text{VH}_n\right)-n\mu_{\text{H}}$ is consistent with Eq.(3). Similar to the temperature dependence of the ΔG^{m} in section S2, the ΔG^{m} in Eq.(3) is also proportional to $k_{\text{B}}T$. Thus, the relatively small ΔG^{m} in Figure 4 in the main text is reasonable and the ΔG^{m} will become more significant at finite temperature than the DFT results at 0K.

S9. Construction of the EAM potential for Cu–H

The EAM potential of Cu developed by Mishin et al.[5] was adopted in the present simulations. The EAM potential of H and the Cu–H cross-pair potential were fitted in the present study. The EAM potentials of H and Cu–H cross-pair potential were parameterized as follows[6].

The embedded energy function [$F(\rho)$] of H is given as

$$F(\rho)=-F_0\left[1-\ln\left(\frac{\rho}{\rho_e}\right)^n\right]\left(\frac{\rho}{\rho_e}\right)^n+F_1\frac{\rho}{\rho_e}, \qquad \textbf{(S3)}$$

where F_0, ρ_e, n, and F_1 are fitting parameters.

The atomic electron density [$f(r)$] of H is given as

$$f(r)=f_e\exp\left[-\chi\left(r-r_e\right)\right]\Psi\left(\frac{r-r_c}{h}\right) \qquad \textbf{(S4)}$$

and

$$\Psi(x)=\begin{cases}\dfrac{x^4}{1+x^4}, & x\le 0\\ 0 & x>0\end{cases}, \qquad \textbf{(S5)}$$

where $\Psi(x)$ is a cutoff function; f_e, χ, and h are fitting parameters; and $r_e = 1.8075$ Å is the distance between an O interstitial site and its nearest-neighboring Cu-atom in an FCC lattice.

The pair potentials [$\phi(r)$] of H–H and H–Cu are given as

$$\phi(r)=\left\{-\alpha\left[1+\beta\left(\frac{r}{r_0}-1\right)\right]\exp\left[-\beta\left(\frac{r}{r_0}-1\right)\right]-\gamma\exp\left[-\kappa\left(\frac{r}{r_0}-1\right)\right]\right\}\Psi\left(\frac{r-r_c}{h}\right), \qquad \textbf{(S6)}$$

where α, β, r_0, γ, κ, r_c, and h are fitting parameters.

The pair potential of $\phi_{\text{H-H}}(r)$ can be set to 0 because the optimized value $r_c = 1$ for the H–H pair potential, which is much less than the minimum distance between H-atoms in the simulations. However, an equivalent two-body interaction between H and H exists in the linear term of the embedding energy of H, $F_1\rho/\rho_e$. The fitted potential parameters are listed in Table I, and the profile of the fitted potential functions is shown in Figure S2.

We used the VASP code for the density functional theory (DFT) computation of the data that is used in the fitting and the validation of the potentials. A $(3 \times 3 \times 3)a_0$ supercell of face-centered cubic (FCC) Cu was adopted, where a_0 = 3.63 Å is the Cu lattice constant computed using the DFT, and a Monkhorst–Pack mesh (4 × 4 × 4) was used for Brillouin-zone integration. The NEB method was employed to calculate the energy barriers of vacancy–Cu exchange.

Table I. Potential parameters of H potential and H–Cu cross-potential.

Embedded energy of H	Value	Pair potential of H–Cu	Value
F_0	3.993680	α	9.090649×10^{-1}
ρ_e	2.000000	β	1.655670×10^{-1}
n	1.491109	r_0	1.889998
F_1	5.213756	γ	-2.652138×10^{-1}
Atomic electron density of H	Value	κ	3.458068
f_e	1.012533×10^{-1}	r_c	2.624089
χ	3.041823	h	1.000000
r_c	4.947559		
h	2.075316×10^{-1}		

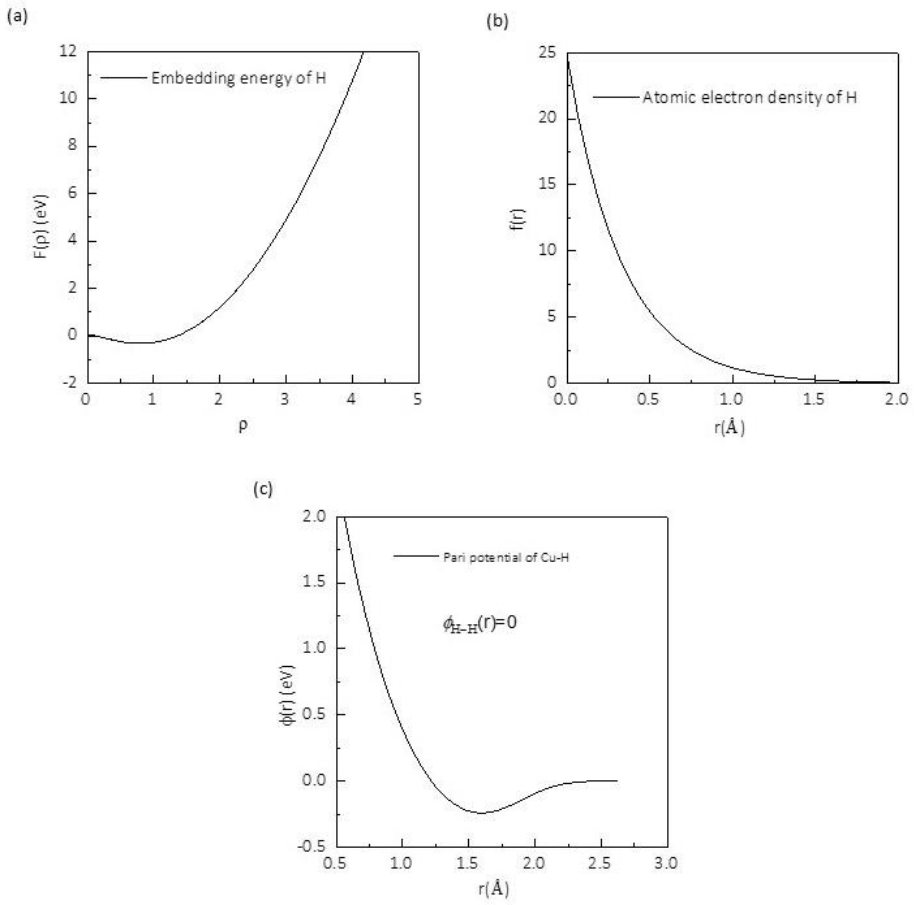

Figure S2. EAM potential of Cu–H. (a) Embedding the energy function, (b) atomic electron density, and (c) pair potential of H and the cross-potential of Cu–H.

The properties used to fit the potentials are outlined as follows.

(1) Site preference

Two types of interstitial sites exist in bulk Cu: O and T sites. For a single vacancy in Cu, there are six O sites and eight T sites encompassing the vacancy. For H trapped in 2NN(O) and 1NN(T) sites near a vacancy, the deviation distances from the central position of a vacancy (off-center distance, see Figure S3), d_O and d_T, given by the DFT calculations, are also used in the fitting. The site preference energy of H on the T and the O sites of bulk Cu is computed as $E_O - E_T$, where

E_O and E_T are the total energies of the bulk Cu with one H occupying O and T sites, respectively. Similarly, the site preference energy of H near a vacancy is computed as $E_{V,O} - E_{V,T}$, where $E_{V,O}$ and $E_{V,T}$ are the total energies of the bulk Cu with one vacancy and one H occupying the 2NN(O) and the 1NN(T) sites near the vacancy, respectively (see Figure S4). According to the DFT calculations, the H-atoms prefer to occupy the O sites rather than the T sites either near the vacancy or in the bulk Cu. The fitting results are listed in Table II. The results of site preference and the off-center distances from the EAM are in good agreement with those from DFT.

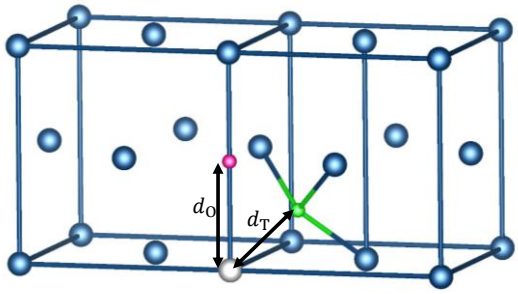

Figure S3. Off-center distance of H. H-atoms occupy O (magenta sphere) and T (green sphere) sites near a vacancy (white sphere) in Cu (blue spheres).

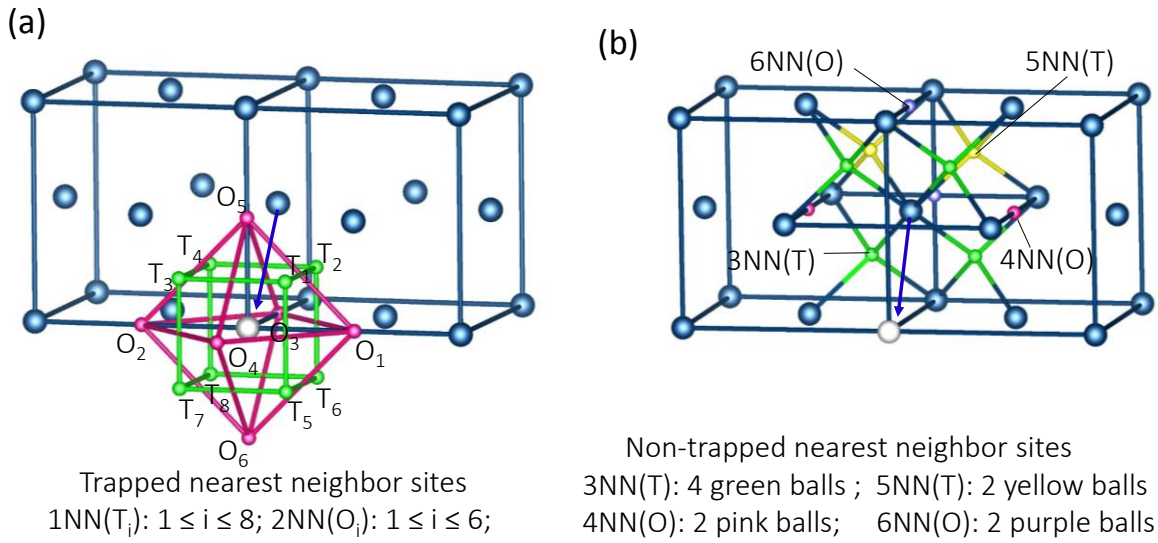

Figure S4. Interstitial sites near a vacancy. (a) 1NN(tetrahedral) (T_1–T_8, green spheres) and 2NN(octahedral) (O_1–O_6, magenta spheres) sites near a vacancy (white sphere) in FCC Cu (blue spheres). (b) 3NN–6NN interstitial sites of vacancies that affect the energy barrier of the diffusion of a Cu-atom (the diffusion direction is indicated by an arrow).

Table II. Properties of H in Cu computed with both DFT and EAM; a_0 is the lattice constant.

	DFT	EAM
d_O (a_0)	0.48	0.49
d_T (a_0)	0.33	0.32
$E_O - E_T$ (eV)	−0.16	−0.17
$E^m_{O\to T}$ (eV)	0.34	0.37
$E^m_{T\to O}$ (eV)	0.20	0.20

(2) Segregation energy of H–vacancy complexes

From the DFT calculations, the segregation energy (ΔE_n^{α}), which is the energy needed to form the $VH_{n,\alpha}$ complex by migration of H-atoms from the O sites in bulk Cu to the sites belonging

to the $VH_{n,\alpha}$ complex, is given by

$\Delta E_n^{\alpha} = E(Cu_{107}VH_{n,\alpha}) + nE(Cu_{108}) - E(Cu_{107}VH_0) - nE(Cu_{108}H_O^b)$, where $E(Cu_{107}VH_{n,\alpha})$, $E(Cu_{107}VH_0)$, $E(Cu_{108}H_O^b)$, and $E(Cu_{108})$ are the energies of a $(3 \times 3 \times 3)$ FCC lattice with a single $VH_{n,\alpha}$ complex, that with a single bare vacancy (VH_0), that with a single H at an O site in bulk Cu (H_O^b), and that of bulk Cu, respectively. The α is used to distinguish the inequivalent VH_n complex. The segregation energies of $VH_{1,1}$, $VH_{1,2}$, $VH_{2,6}$, $VH_{2,7}$, $VH_{2,3}$, $VH_{2,4}$, $VH_{2,5}$, and $VH_{6,1}$ in Table III are used in the fitting. The fitting results are also shown in Figure S5. The results from EAM are in agreement with those from DFT.

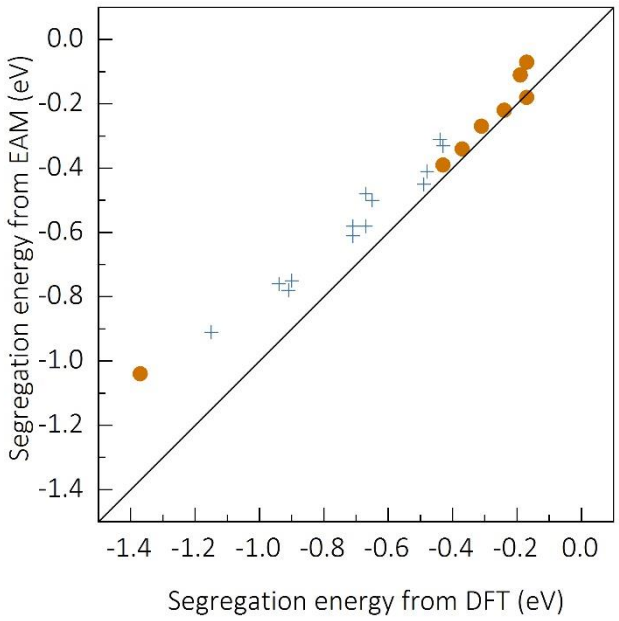

Figure S5. Segregation energy of the VH_n complex given by DFT and EAM potential. The solid line denotes the positions where the values from EAM are equal to those from DFT. The orange symbols denote the data used in fitting the EAM potential.

The properties used to validate the potential are outlined as follows.

(1) Energy barrier for diffusion of H in Cu

The energy barrier for H diffusion in Cu was computed using the nudged elastic band (NEB) method. The calculated barriers for the diffusion of a H-atom from an O site to a neighboring T site ($E^{\mathrm{m}}_{\mathrm{O}\to\mathrm{T}}$) and the reversion ($E^{\mathrm{m}}_{\mathrm{T}\to\mathrm{O}}$) in the bulk Cu computed with the present EAM are in good agreement with those obtained from DFT (see Table II).

(2) Segregation Energy of H–vacancy complex

The segregation energies of $VH_{n,\alpha}$ complexes (configurations listed in Table III) computed with the present EAM potential are shown in Figure S5, where they are compared with those obtained from DFT. Figure S5 shows that the results of segregation energies of VH_n complexes obtained from the EAM are in good agreement with those obtained from DFT for $n < 4$. The segregation energies of VH_5 and VH_6 complexes obtained from EAM are in reasonable agreement with those from DFT.

Table III. Inequivalent configurations of $VH_{n,\alpha}$ complexes and the corresponding segregation energy ΔE_n^{α} computed with both DFT and EAM. The specific interstitial sites occupied by H are listed in the parentheses following $VH_{n,\alpha}$, and the positions of the eight 1NN(T_i) ($1 \le i \le 8$) and six 2NN(O_i) ($1 \le i \le 6$) sites are shown in Figure S3.

Configuration	*n*	α	DFT	EAM
$VH_{1,1}(O_1)$	1	1	-0.24	-0.22
$VH_{1,2}(T_1)$	1	2	-0.17	-0.18
$VH_{2,1}(O_1O_2)$	2	1	-0.49	-0.45
$VH_{2,2}(O_1O_3)$	2	2	-0.48	-0.41
$VH_{2,3}(T_1T_2)$	2	3	-0.17	-0.07
$VH_{2,4}(T_1T_4)$	2	4	-0.31	-0.27
$VH_{2,5}(T_1T_6)$	2	5	-0.37	-0.34
$VH_{2,6}(O_1T_1)$	2	6	-0.19	-0.11
$VH_{2,7}(O_1T_3)$	2	7	-0.43	-0.39
$VH_{3,1}(O_1O_2O_3)$	3	1	-0.71	-0.61
$VH_{3,2}(O_1O_3O_5)$	3	2	-0.71	-0.58
$VH_{3,3}(O_1O_3T_1)$	3	3	-0.44	-0.31
$VH_{3,4}(O_1O_3T_3)$	3	4	-0.67	-0.58
$VH_{3,5}(O_1O_2T_1)$	3	5	-0.43	-0.33
$VH_{4,1}(O_1O_2O_3O_4)$	4	1	-0.91	-0.78
$VH_{4,2}(O_1O_2O_3O_5)$	4	2	-0.94	-0.76
$VH_{4,3}(O_1O_2O_3T_1)$	4	3	-0.65	-0.50
$VH_{4,4}(O_1O_3O_5T_5)$	4	4	-0.90	-0.75
$VH_{4,5}(O_1O_3O_5T_3)$	4	5	-0.67	-0.48
$VH_{5,1}(O_1O_2O_3O_4O_5)$	5	1	-1.15	-0.91
$VH_{6,1}(O_1O_2O_3O_4O_5O_6)$	6	1	-1.37	-1.04

(3) Energy barrier for the diffusion of H–vacancy complex

The barrier energies of the diffusion pathway of H–vacancy complexes (95 configurations listed in Table IV) were computed with the present EAM potential in comparison with those obtained from DFT. The configurations of the 95 H–vacancy complexes include two categories (see Table IV). One category is that only 1NN(T) and 2NN(O) sites are occupied by the H-atoms. The other category is created by adding one additional H on the 3NN~6NN sites, whose saddle configuration

mimics the H–vacancy configurations at the saddle state considering the chemical composition variation of H along the diffusion pathway. Figure S6 shows that the energy barrier obtained from EAM is in good agreement with those obtained from DFT. The present potential can be used to study the diffusivity of the H–vacancy complex in Cu.

Table IV. Inequivalent diffusion pathway for (a) $VH_{n,\alpha}$ +H_1(O_{4NN} / O_{6NN}) and (b) $VH_{n,\alpha}$ +H_1(T_{3NN} / T_{5NN}) complexes computed with both DFT and EAM. The specific sites occupied by H are listed in the parentheses following $VH_{n,\alpha}$ and H_1. The positions of the eight 1NN(T_i) ($1 \le i \le 8$) and six 2NN(O_i) ($1 \le i \le 6$) sites are shown in Figure S4(a). O_{4NN}, O_{6NN}, T_{3NN}, and T_{5NN} in the parentheses denote that only one H occupies the 3NN–6NN O/T interstitial site, as shown in Figure S4(b).

(a)

Configuration VH_n,	$VH_{n,\alpha}$		$VH_{n,\alpha}$ +H_1(O_{4NN})		$VH_{n,\alpha}$ +H_1(O_{6NN})	
	DFT	EAM	DFT	EAM	DFT	EAM
$VH_{0,1}$	0.72	0.69	0.62	0.67	0.53	0.54
$VH_{1,1}(O_1)$	0.83	0.82	0.75	0.80	0.63	0.64
$VH_{1,2}(O_3)$	0.89	0.82	0.78	0.77	0.68	0.66
$VH_{1,3}(O_4)$	0.77	0.74	0.67	0.72	0.56	0.59
$VH_{2,1}(O_1O_2)$	0.95	0.94	0.88	0.92	0.74	0.80
$VH_{2,2}(O_3O_4)$	0.97	0.88	0.84	0.83	0.75	0.72
$VH_{2,3}(O_4O_6)$	0.83	0.81	0.71	0.78	0.61	0.64
$VH_{2,4}(O_1O_4)$	0.88	0.87	0.79	0.84	0.67	0.71
$VH_{2,5}(O_3O_6)$	0.93	0.86	0.81	0.81	0.70	0.70
$VH_{2,6}(O_1O_3)$	1.00	0.93	0.89	0.88	0.78	0.77
$VH_{2,7}(O_3O_5)$	1.25	1.05	1.14	0.95	1.03	0.87
$VH_{3,1}(O_1O_2O_3)$	1.11	1.06	1.00	1.01	0.88	0.89
$VH_{3,2}(O_1O_2O_6)$	0.98	1.00	0.89	0.97	0.77	0.84
$VH_{3,3}(O_1O_3O_4)$	1.05	1.00	0.92	0.93	0.82	0.82
$VH_{3,4}(O_1O_3O_5)$	1.35	1.13	1.24	1.03	1.12	0.94
$VH_{3,5}(O_1O_3O_6)$	1.02	0.98	0.90	0.91	0.79	0.81
$VH_{3,6}(O_1O_4O_6)$	0.92	0.93	0.81	0.90	0.70	0.77
$VH_{3,7}(O_3O_4O_5)$	1.29	1.09	1.16	0.99	1.06	0.90
$VH_{3,8}(O_4O_5O_6)$	0.99	0.93	0.85	0.87	0.76	0.75
$VH_{4,1}(O_1O_2O_3O_5)$	1.46	1.26	1.37	1.16	1.23	1.07
$VH_{4,2}(O_1O_2O_4O_5)$	1.13	1.10	1.03	1.04	0.93	0.92
$VH_{4,3}(O_1O_2O_4O_6)$	1.05	1.06	0.94	1.02	0.82	0.89
$VH_{4,4}(O_1O_2O_5O_6)$	1.16	1.12	1.04	1.05	0.95	0.94
$VH_{4,5}(O_2O_3O_5O_6)$	1.39	1.17	1.28	1.11	1.15	0.97

$VH_{4,6}(O_2O_4O_5O_6)$	1.08	1.04	0.96	0.98	0.86	0.86
$VH_{4,7}(O_3O_4O_5O_6)$	1.32	1.14	1.18	1.02	1.07	0.94
$VH_{5,1}(O_1O_2O_3O_5O_6)$	1.50	1.29	1.37	1.19	1.25	1.10
$VH_{5,2}(O_1O_2O_4O_5O_6)$	1.20	1.16	1.08	1.09	0.98	0.98
$VH_{5,3}(O_2O_3O_4O_5O_6)$	1.42	1.21	1.31	1.14	1.18	1.01
$VH_{6,1}(O_1O_2O_3O_4O_5O_6)$	1.54	1.33	1.42	1.23	1.30	1.13

(b)

Configuration	$VH_{n,\alpha}$		$VH_{n,\alpha}$ +$H_1(O_{3NN})$		$VH_{n,\alpha}$ +$H_1(O_{5NN})$	
VH_n,	DFT	EAM	DFT	EAM	DFT	EAM
$VH_{0,1}$			0.43	0.43	0.42	0.47
$VH_{1,1}(T_1)$	0.78	0.69				
$VH_{1.2}(T_2)$*	Unstable	Unstable				
$VH_{1,3}(T_5)$	0.76	0.78				

*H at a T_2 site is unstable during the vacancy–Cu exchange.

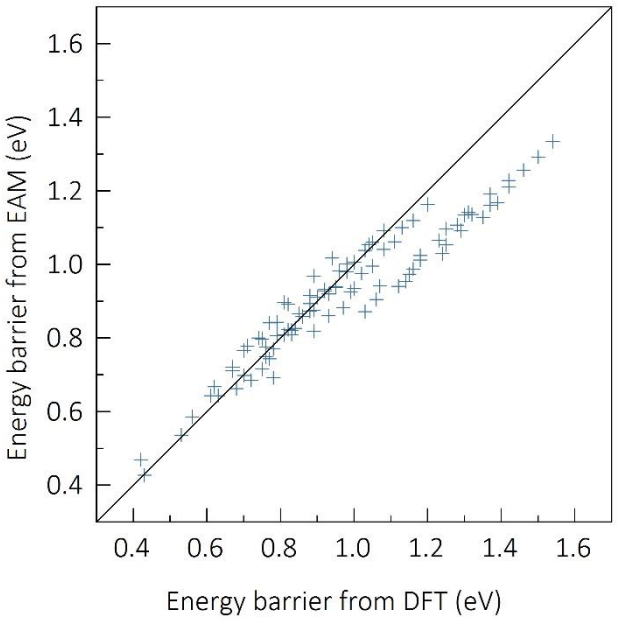

Figure S6. Energy barrier (eV) of H–vacancy complex diffusion given by DFT and EAM. The solid line denotes the positions where the values from EAM are equal to those from DFT.

(4) Segregation energy of one H on different interstitial sites in the initial and the saddle state of the vacancy diffusion at 0 K

In an FCC Cu lattice with a single vacancy, eight 1NN(T) and six 2NN(O) interstitial sites are located near the vacancy (see Figure S4(A)); one interstitial H can occupy each site. We carried out vacancy segregation energy calculations using both the DFT and the EAM to confirm that the H-atoms in 1NN(T) and 2NN(O) sites of the initial state of vacancy diffusion are strongly bound (see Figure S7). However, for the H-atoms located beyond 2NN from the vacancy, the H–vacancy interaction becomes weak and can be ignored. For the saddle state of vacancy diffusion, the segregation energy of H-atoms was calculated using the saddle configuration of vacancy–Cu exchange under the constraint that the relative displace vector between the exchanged Cu atom and the center of mass of the reminding Cu atoms is fixed. Meanwhile, the equivalent interstitial sites for H occupying, such as the eight 2NN(O) sites, becomes inequivalent. Figure S8 shows the segregation energy of the 2NN(O), the 4NN(O) and the 6NN(O) sites at the saddle state using both the DFT and the EAM. We can see from Figure S8 that the ability of adsorbing H of the 2NN(O) sites decreases comparing with those at the initial state. The closer to the jumping Cu, the weaker the ability attracting H, that is $O_4=O_6>O_1=O_2>O_3=O_5$. While the ability adsorbing H of the 4NN(O) and the 6NN(O) sites are enhanced at the saddle state comparing to those at the initial state. Specially, the two 4NN(O) and the two 6NN(O) sites are, respectively, equivalent to the O_1/O_2 and the O_4/O_6 sites at the saddle state. Furthermore, the 4NN(O) and the 6NN(O) sites will be translated to 2NN(O) sites at the final state of the vacancy diffusion. Similarly, the four 3NN(T) and the two 5NN(T) sites in the initial state can also adsorb H atoms at the saddle state, and these interstitial sites will be translated to 1NN(T) sites at the final state of vacancy diffusion. Thus, the H atoms on the 1NN(T) and 2NN(O) sites with respect to the vacancy center in the initial state can

be viewed as the adsorbed H atoms, while the H atoms on the 1NN(T) and 2NN(O) sites with respect to the vacancy centers of either the initial or the final state can be viewed as the adsorbed H atoms at the saddle state.

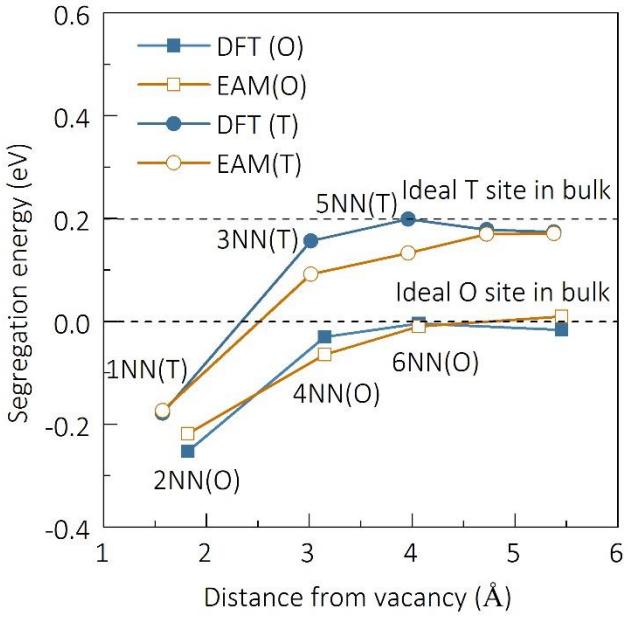

Figure S7. Segregation energy of one H on different interstitial sites near a vacancy. The segreagtion energies are calculated using H on an O site of FCC Cu as a reference state, as computed with DFT and EAM. The dashed lines denote the ideal segregation energy of H on O or T sites in bulk FCC Cu.

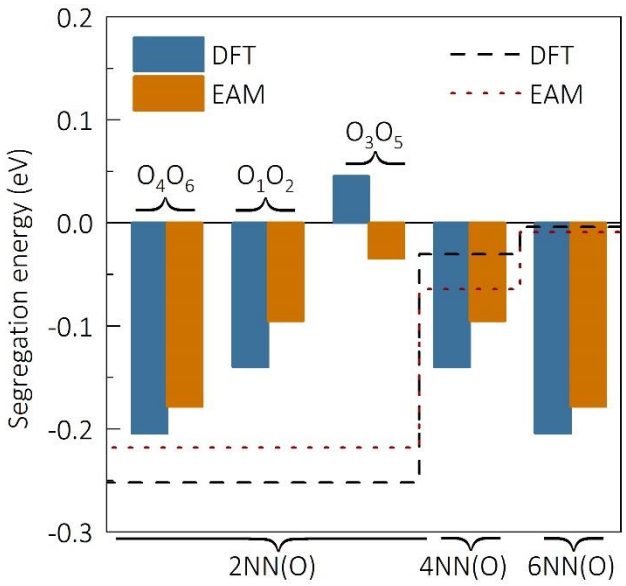

Figure S8. Segregation energy of one H on the different interstitial sites at the saddle state of the vacancy diffusion, as computed with DFT and EAM. The specific symbols of the interstitial sites is referred in Figure S4. For comparison, the segregation energies at the initial state are shown by the dash and dot lines for the DFT and EAM, respectively.

(5) Energy of the configurations in the initial and the saddle states at finite temperature

To validate the accuracy of the EAM potential in the MD simulation, we compare the energies of the atomic configurations created from a constrained-MD simulation computed using the EAM to those using the DFT. The model size used in the constrained-MD simulation is (3 × 3 × 3) FCC lattice Cu with a vacancy and 20 H-atoms. The constrained-MD simulations using the EAM were performed for 200 ps at 870 K, respectively, for the initial and the saddle states of the vacancy diffusion. The atomic configurations are sampled every 2 ps, so that 100 atomic configurations are given for the initial and the final states, respectively. Using the first configuration at the initial state as a reference, the relative energy variance of the configurations are show in Figure S9 for both

the EAM and the DFT. From Figure S9, the relative energies computed from EAM is in good agreement with those from DFT at 870 K.

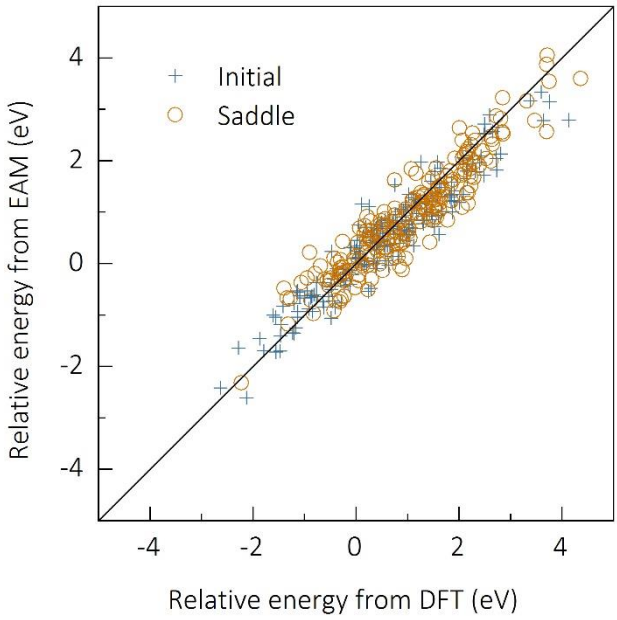

Figure S9. Energy of the model, $Cu_{107}VH_{20}$, in the initial and the saddle state at 870 K. The energies are calculated using the first configuration as a reference state, as computed by DFT and EAM.

References

(1) Den Otter, W. K.; Briels, W. J. Free Energy from Molecular Dynamics with Multiple Constraints. *Mol. Phys.* **2000**, *98*, 773–781.

(2) Daw, M. S.; Baskes, M. I. Semiempirical, Quantum Mechanical Calculation of Hydrogen Embrittlement in Metals. *Phys. Rev. Lett.* **1983**, *50*, 1285–1288.

(3) Daw, M. S.; Baskes, M. I. Embedded-Atom Method: Derivation and Application to Impurities, Surfaces, and Other Defects in Metals. *Phys. Rev. B* **1984**, *29*, 6443–6453.

(4) Foiles, S. M.; Baskes, M. I.; Daw, M. S. Embedded-Atom-Method Functions for the Fcc Metals Cu, Ag, Au, Ni, Pd, Pt, and Their Alloys. *Phys. Rev. B* **1986**, *33*, 7983–7991.

(5) Mishin, Y.; Mehl, M. J.; Papaconstantopoulos, D. A.; Voter, A. F.; Kress, J. D. Structural Stability and Lattice Defects in Copper: Ab Initio, Tight-Binding, and Embedded-Atom Calculations. *Phys. Rev. B* **2001**, *63*, 224106.

(6) Du, J. P.; Wang, C. Y.; Yu, T. Construction and Application of Multi-Element EAM Potential (Ni-Al-Re) in γ/γ′ Ni-Based Single Crystal Superalloys. *Modell. Simul. Mater. Sci. Eng.* **2013**, *21*, 015007.

(7) Zhou, X. W.; Zimmerman, J. A.; Wong, B. M.; Hoyt, J. J. An Embedded-Atom Method Interatomic Potential for Pd–H Alloys. *J. Mater. Res.* **2008**, *23*, 704–718.

(8) Henkelman, G.; Uberuaga, B. P.; Jónsson, H. A Climbing Image Nudged Elastic Band Method for Finding Saddle Points and Minimum Energy Paths. *J. Chem. Phys.* **2000**, *113*, 9901–9904.

(9) Ciccotti, G.; Kapral, R.; Sergi, A. Non-Equilibrium Molecular Dynamics. *Handbook of Materials Modeling*; Springer: Berlin, 2005; pp 745–761.

(10) Plimpton, S. Fast Parallel Algorithms for Short-Range Molecular Dynamics. *J. Comput. Phys.* **1995**, *117*, 1–19.

(11) Kresse, G.; Hafner, J. Ab Initio Molecular Dynamics for Liquid Metals. *Phys. Rev. B* **1993**, *47*, 558–561.

(12) Kresse, G.; Hafner, J. Ab Initio Molecular-Dynamics Simulation of the Liquid-Metal–amorphous-Semiconductor Transition in Germanium. *Phys. Rev. B* **1994**, *49*, 14251–14269.

(13) Kresse, G.; Furthmüller, J. Efficient Iterative Schemes for Ab Initio Total-Energy Calculations Using a Plane-Wave Basis Set. *Phys. Rev. B* **1996**, *54*, 11169–11186.

(14) Kresse, G.; Joubert, D. From Ultrasoft Pseudopotentials to the Projector Augmented-Wave Method. *Phys. Rev. B* **1999**, *59*, 1758–1775.

(15) Perdew, J. P.; Burke, K.; Ernzerhof, M. Generalized Gradient Approximation Made Simple. *Phys. Rev. Lett.* **1996**, *77*, 3865–3868.

(16) Touloukian, Y.; Kirby, R. K.; Talor, R. E.; Desai, P. D. *Thermophysical Properties of Matter, V. 12: Thermal Expansion Metallic Elements and Alloys*; Plenum: New York; 1975.

(17) Mehrer, H. *Diffusion in Solids: Fundamentals, Methods, Materials, Diffusion-Controlled Processes*; Springer: Berlin; 2007.

(18) Kirchheim, R.; Somerday, B.; Sofronis, P. Chemomechanical Effects on the Separation of Interfaces Occurring during Fracture with Emphasis on the Hydrogen-Iron and Hydrogen-Nickel System. *Acta Mater.* **2015**, *99*, 87–98.